

## Article

# Structural and Mechanistic Basis for the Inactivation of Human Ornithine Aminotransferase by (3S,4S)-3-Amino-4-fluorocyclopentenecarboxylic Acid

Sida Shen <sup>1,†</sup>, Arseniy Butrin <sup>2,†</sup>, Brett A. Beaupre <sup>2</sup>, Glaucio M. Ferreira <sup>3</sup>, Peter F. Doubleday <sup>4,5</sup>, Daniel H. Grass <sup>1</sup>, Wei Zhu <sup>1</sup>, Neil L. Kelleher <sup>1,4,5</sup>, Graham R. Moran <sup>2</sup>, Dali Liu <sup>2,\*</sup> and Richard B. Silverman <sup>1,4,6,\*</sup>

<sup>1</sup> Department of Chemistry and Center for Developmental Therapeutics, Northwestern University, Evanston, IL 60208, USA

<sup>2</sup> Department of Chemistry and Biochemistry, Loyola University Chicago, Chicago, IL 60660, USA

<sup>3</sup> Department of Clinical and Toxicological Analyses, School of Pharmaceutical Sciences, University of São Paulo, São Paulo 05508-000, SP, Brazil

<sup>4</sup> Department of Molecular Biosciences, Northwestern University, Evanston, IL 60208, USA

<sup>5</sup> Proteomics Center of Excellence, Northwestern University, Evanston, IL 60208, USA

<sup>6</sup> Department of Pharmacology, Northwestern University, Chicago, IL 60611, USA

\* Correspondence: dliu@luc.edu (D.L.); r-silverman@northwestern.edu (R.B.S.);

Tel.: +1-773-508-3093 (D.L.); +1-847-491-5653 (R.B.S.)

† These authors contributed equally to this work.

**Abstract:** Ornithine aminotransferase (OAT) is overexpressed in hepatocellular carcinoma (HCC), and we previously showed that inactivation of OAT inhibits the growth of HCC. Recently, we found that (3S,4S)-3-amino-4-fluorocyclopentenecarboxylic acid (**5**) was a potent inactivator of  $\gamma$ -aminobutyric acid aminotransferase (GABA-AT), proceeding by an enamine mechanism. Here we describe our investigations into the activity and mechanism of **5** as an inactivator of human OAT. We have found that **5** exhibits 10-fold less inactivation efficiency ( $k_{\text{inact}}/K_i$ ) against *h*OAT than GABA-AT. A comprehensive mechanistic study was carried out to understand its inactivation mechanism with *h*OAT.  $pK_a$  and electrostatic potential calculations were performed to further support the notion that the  $\alpha,\beta$ -unsaturated alkene of **5** is critical for enhancing acidity and nucleophilicity of the corresponding intermediates and ultimately responsible for the improved inactivation efficiency of **5** over the corresponding saturated analogue (**4**). Intact protein mass spectrometry and the crystal structure complex with *h*OAT provide evidence to conclude that **5** mainly inactivates *h*OAT through noncovalent interactions, and that, unlike with GABA-AT, covalent binding with *h*OAT is a minor component of the total inhibition which is unique relative to other monofluoro-substituted derivatives. Furthermore, based on the results of transient-state measurements and free energy calculations, it is suggested that the  $\alpha,\beta$ -unsaturated carboxylate group of PLP-bound **5** may be directly involved in the inactivation cascade by forming an enolate intermediate. Overall, compound **5** exhibits unusual structural conversions which are catalyzed by specific residues within *h*OAT, ultimately leading to an enamine mechanism-based inactivation of *h*OAT through noncovalent interactions and covalent modification.

**Keywords:** aminotransferase; mechanism-based inactivators; enamine; cyclopentene; mechanistic studies

**Citation:** Shen, S.; Butrin, A.; Beaupre, B.A.; Ferreira, G.M.; Doubleday, P.F.; Grass, D.H.; Zhu, W.; Kelleher, N.L.; Moran, G.R.; Liu, D.; et al. Structural and Mechanistic Basis for the Inactivation of Human Ornithine Aminotransferase by (3S,4S)-3-Amino-4-fluorocyclopentenecarboxylic Acid. *Molecules* **2023**, *28*, 1133. <https://doi.org/10.3390/molecules28031133>

Academic Editor: Elisa Nuti

Received: 20 December 2022

Revised: 16 January 2023

Accepted: 17 January 2023

Published: 23 January 2023



**Copyright:** © 2023 by the authors. Licensee MDPI, Basel, Switzerland. This article is an open access article distributed under the terms and conditions of the Creative Commons Attribution (CC BY) license (<https://creativecommons.org/licenses/by/4.0/>).

## 1. Introduction

Aminotransferases are members of the pyridoxal 5'-phosphate (PLP)-dependent class of enzymes. They are capable of performing two coupled transamination reactions between an amino acid and an  $\alpha$ -keto acid, participating in essential nitrogen metabolism in vivo [1]. The PLP moiety links to a catalytic lysine (Lys) residue through a Schiff base, forming an internal PLP-Lys aldimine structure, which can specifically react with an amino acid substrate to produce a keto analog while forming pyridoxamine 5'-phosphate (PMP), thereby completing the first transamination reaction. The PMP then forms another Schiff base with an  $\alpha$ -keto acid substrate during the second transamination reaction catalyzed by the aminotransferase to generate an  $\alpha$ -amino acid and the original internal PLP-Lys aldimine cofactor [2].

Several aminotransferases have been recognized as therapeutic targets for neurological disorders and cancers. For example,  $\gamma$ -aminobutyric acid aminotransferase (GABA-AT, E.C. 2.6.1.19) functions to degrade the primary inhibitory neurotransmitter GABA to succinic semialdehyde (SSA) (Figure 1A) while producing the major excitatory neurotransmitter L-glutamate (L-Glu) from  $\alpha$ -ketoglutarate ( $\alpha$ -KG) [3]. The inhibition of GABA-AT has emerged as a therapeutic approach for epilepsy which acts by balancing the reduced GABA levels detected in these patients' central nervous systems [4]. Human ornithine  $\delta$ -aminotransferase (*hOAT*; EC2.6.1.13), which belongs to the same evolutionary subgroup as GABA-AT, converts L-ornithine (L-Orn) into L-glutamate- $\gamma$ -semialdehyde (L-GSA) while also producing L-Glu from  $\alpha$ -KG (Figure 1B) [5]. We previously found that the *OAT* gene was overexpressed in spontaneous hepatocellular carcinoma (HCC)-developing livers from sand rats [6]. Moreover, pharmacological inhibition of *hOAT* significantly inhibited tumor growth in an HCC mouse model [6]. A recent study also revealed that *hOAT* knockdown suppressed the tumor growth in a non-small cell lung cancer (NSCLC) mouse model [7]. Consequently, *hOAT* has emerged as a potential target for developing effective treatments for different types of cancers; therefore, we are interested in determining the mechanistic differences among compounds that inactivate both GABA-AT and *hOAT* for the future design of selective inactivators of either GABA-AT or *hOAT* as potential therapeutics.

To date, vigabatrin (VGA,  $\gamma$ -vinyl-GABA, Scheme 1) is the only FDA-approved GABA-AT inhibitor for the treatment of infantile spasms that acts as a mechanism-based inactivator (MBI) [3,8]. MBIs initially react in a similar manner to substrates in the active site of the targeted enzymes and are converted into an activated species, which usually leads to inactivation either by covalent bond formation or tight-binding inhibition [9]. Mechanistic and crystallographic studies have demonstrated that 70% of vigabatrin inactivation of GABA-AT occurs through a Michael addition pathway: after deprotonation (**M1** to **M2**) and tautomerization (**M2** to **M3**) steps, electrophile **M3** reacts with the catalytic Lys329 residue in GABA-AT to form a covalent bond (**M4** and **M5**). Thirty percent of vigabatrin's inactivation occurs via tautomerization of the vinyl group (**M2** to **M6**); an attack by Lys329 generates enamine intermediate **M7**. This reacts with the internal PLP-Lys329 aldimine, leading to inactivated complex **M8** (Scheme 1) [10].

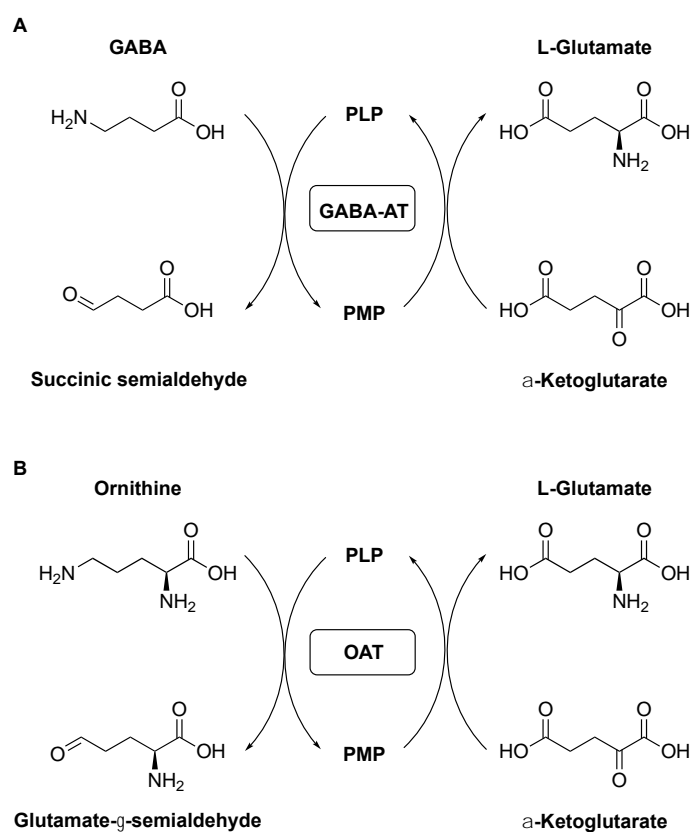
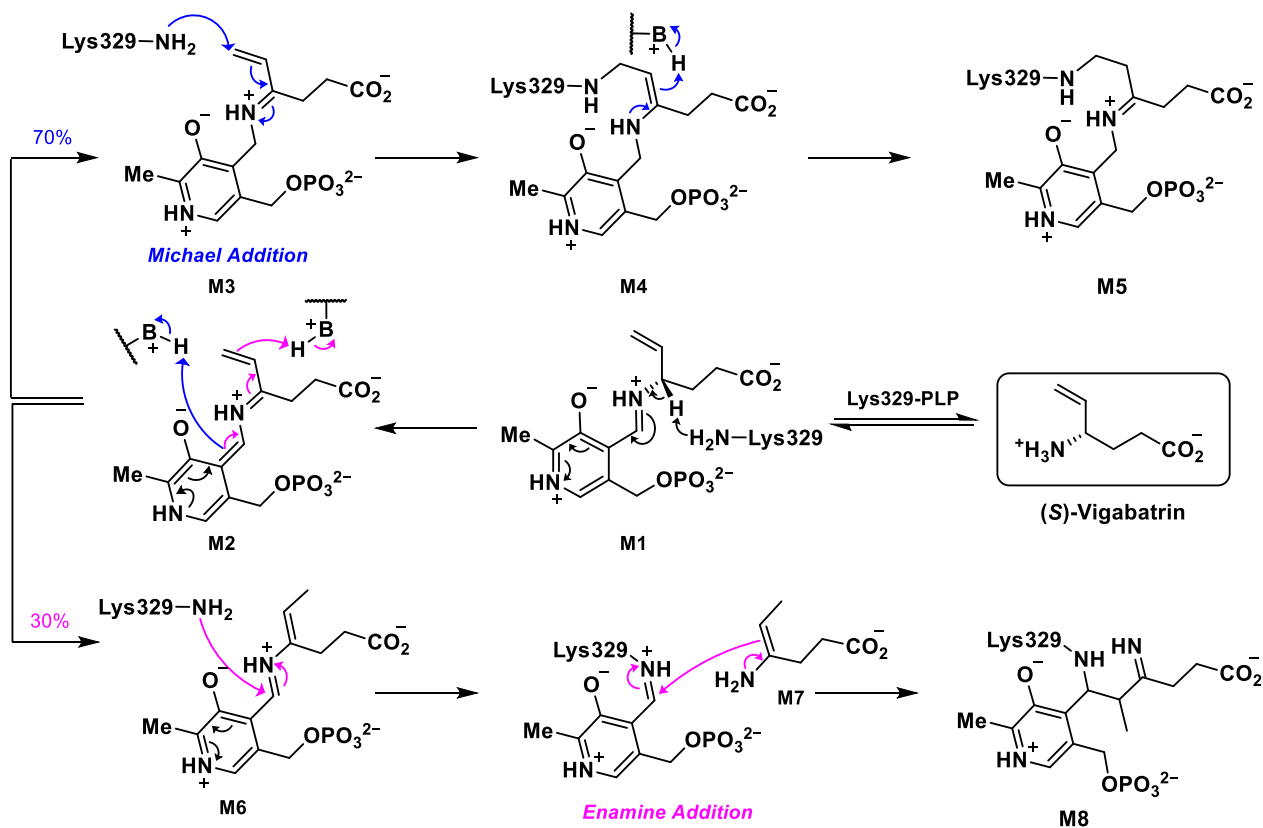
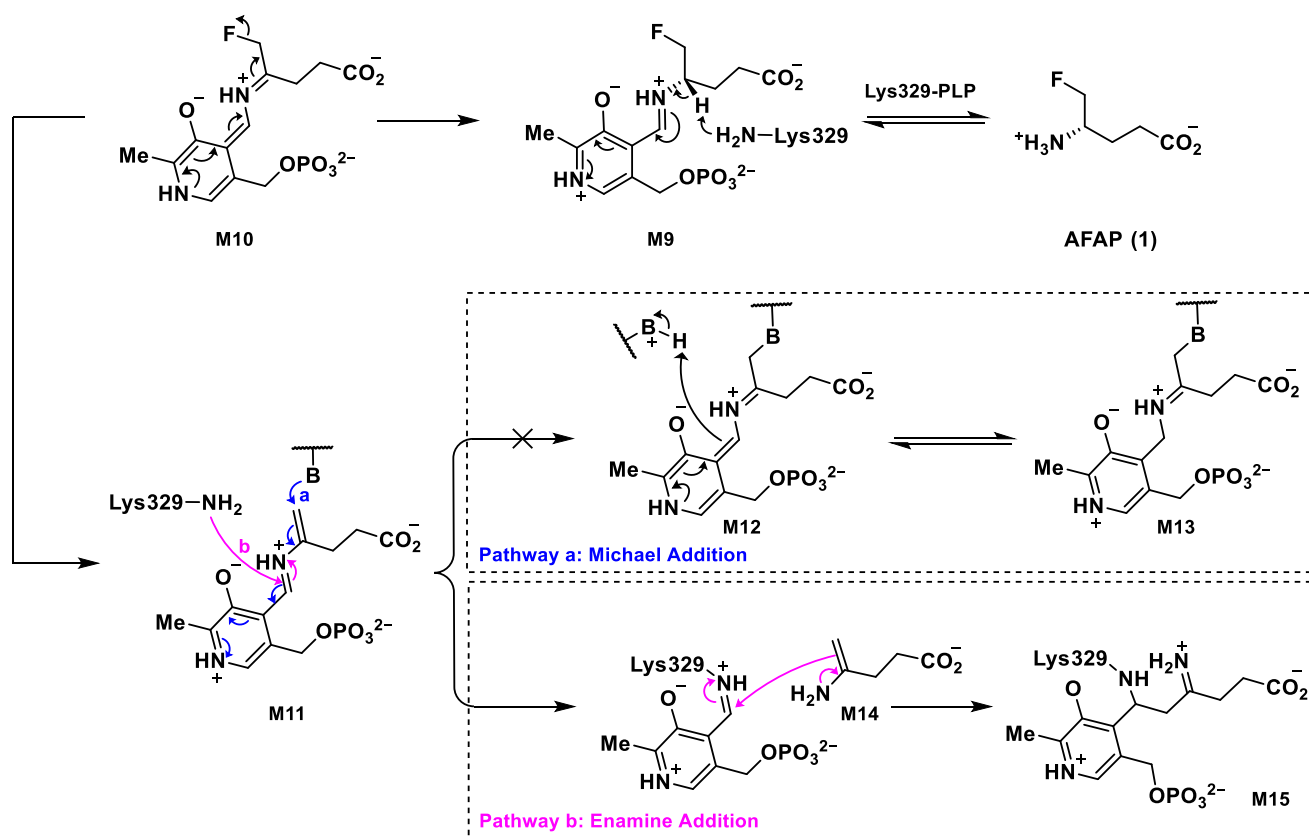


Figure 1. Coupled transamination reactions of GABA-AT (A) and OAT (B).

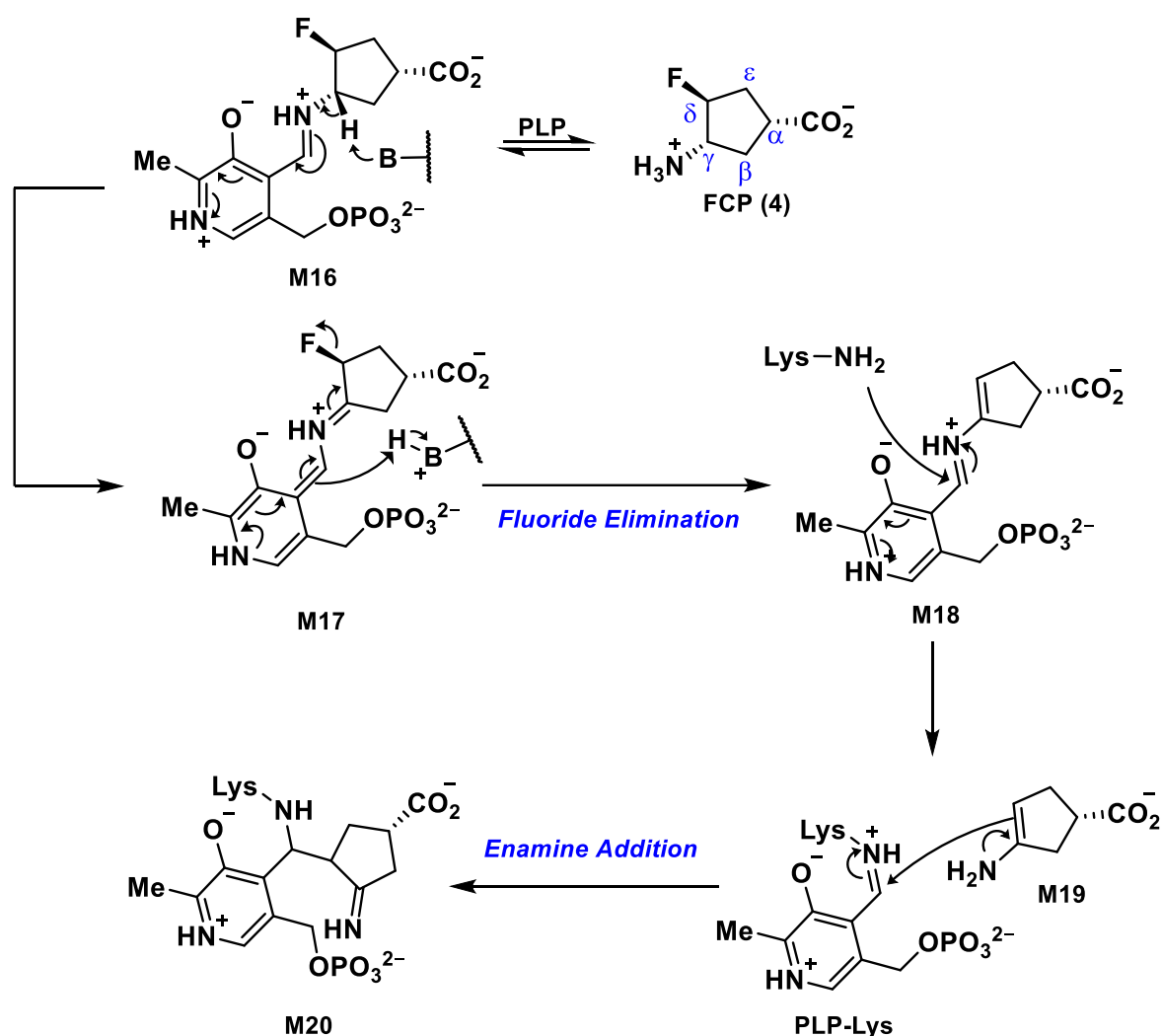


Scheme 1. Mechanisms of inactivation of GABA-AT by (S)-vigabatrin.

Inspired by the inactivation mechanism of vigabatrin, (*S*)-4-amino-5-fluoropentanoic acid **1**, AFPA) was initially designed as a Michael addition mechanism-based GABA-AT inactivator [11]. After deprotonation (**M9** to **M10**) and fluoride ion elimination (**M10** to **M11**), it was anticipated that electrophile **M11** would form **M12** then **M13** from nucleophilic attack by an active site residue (Pathway a; Scheme 2). However, subsequent mechanistic studies revealed that the Lys329 residue reacts exclusively with the imine linkage of **M11**, releasing enamine intermediate **M14** and forming covalently bound **M15** (Pathway b; Scheme 2) [12]. Therefore, AFPA inactivates GABA-AT through an enamine addition mechanism rather than via the initially proposed Michael addition. Since this discovery, a number of alkyl chain and cyclized analogs bearing a monofluoro group have been demonstrated to be enamine addition MBIs of GABA-AT or *h*OAT (Table 1) [13–17]. Because of the structural similarity between GABA-AT and *h*OAT, cyclopentane-based FCP (**4**) was found to exhibit dual inactivation of these two aminotransferases via the same enamine inactivation mechanism (Scheme 3) [18]. Similar to the enamine addition pathway of AFPA (Pathway b; Scheme 2), the inactivation mechanism of FCP is initiated by the formation of Schiff base **M16**, followed by deprotonation (**M16** to **M17**) and fluoride ion elimination (**M17** to **M18**) to afford intermediate **M18**. The released enamine intermediate **M19** from **M18** reacts with the internal PLP–Lys aldimine to yield the covalent adduct **M20**, whose structure was verified by crystallography and intact protein mass spectrometry (intact protein MS) [13,18,19].



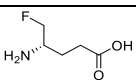
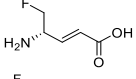
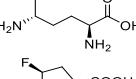
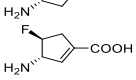
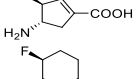
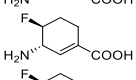
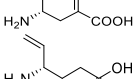
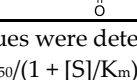
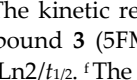
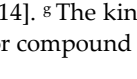
**Scheme 2.** Michael addition and enamine inactivation mechanisms of AFPA (**1**).



**Scheme 3.** The enamine addition inactivation mechanism of FCP (4) in GABA-AT and hOAT.

By incorporation of a double bond into the C $_{\alpha}$  and C $_{\beta}$  positions of FCP (4) (Scheme 3), we recently found that cyclopentene derivative **5** showed 23-fold improved inactivation efficiency ( $k_{\text{inact}}/K_i$ ) against GABA-AT (Table 1) [13]. When **5** was tested against hOAT, a 9.5-fold increase in inactivation efficiency was observed relative to **4**. This indicates that **5** has the potential for multiple therapeutic activities by the inactivation of both GABA-AT and hOAT. In this paper, we synthesized and evaluated another cyclopentene derivative (**6**) bearing an  $\alpha,\epsilon$ -conjugated carboxylate. In addition, we utilized computational calculations to elucidate the effects of slight structural differences among **4–6** on their inactivation steps, which eventually influence their inhibitory activities. We also carried out mechanistic studies of **5** with hOAT using intact MS, transient-state kinetics, and co-crystallization to reveal that compound **5** primarily inactivates hOAT through an unusual noncovalent interaction.

**Table 1.** Kinetic constants for the inhibition of *h*OAT and GABA-AT by 1–9 and (*S*)-vigabatrin <sup>a</sup>.

Cmpd	Structure	<i>h</i> OAT			GABA-AT		
		<i>K<sub>i</sub></i> (mM)	<i>k<sub>inact</sub></i> (min <sup>−1</sup> )	<i>k<sub>inact</sub>/K<sub>i</sub></i> (min <sup>−1</sup> mM <sup>−1</sup> )	<i>K<sub>i</sub></i> (mM)	<i>k<sub>inact</sub></i> (min <sup>−1</sup> )	<i>k<sub>inact</sub>/K<sub>i</sub></i> (min <sup>−1</sup> mM <sup>−1</sup> )
<b>1 (AFPA)</b> <sup>b</sup>		0.23	0.17	0.75	0.40	0.5	1.27
<b>2</b> <sup>c</sup>			NT				0.12
<b>3 (5FMOrn)</b> <sup>d</sup>		0.03	0.17 <sup>e</sup>	5.8		NT	
<b>4 (FCP)</b> <sup>f</sup>		1.4	0.086	0.06	0.078	0.017	0.22
<b>5</b> <sup>g</sup>		0.25	0.143	0.57	0.026	0.132	5.08
<b>6</b>		No inhibition up to 10 mM			<i>K<sub>i</sub></i> = 0.10 mM		
<b>7</b> <sup>h</sup>			NT		No inhibition up to 10 mM		
<b>8</b> <sup>f</sup>		0.031	0.075	2.41	1.1	0.20	0.18
<b>9</b> <sup>f</sup>		4.38	0.075	0.017	4.28	0.028	0.0065
<b>VGA</b>		<i>K<sub>i</sub></i> = 46 mM			0.29	0.21	0.73

<sup>a</sup> *k<sub>inact</sub>* and *K<sub>i</sub>* values were determined by the equation:  $k_{obs} = k_{inact} \times [(K_i + [I])]$ ; *K<sub>i</sub>* was calculated by the equation:  $K_i = IC_{50}/(1 + [S]/K_m)$ ; NT, not tested. <sup>b</sup> The kinetic results for compound 1 were taken from reference [6]. <sup>c</sup> The kinetic results for compound 2 were taken from reference [20]. <sup>d</sup> The kinetic results for compound 3 (5FMOrn) were taken from reference [21]. <sup>e</sup> *k<sub>inact</sub>* was calculated by the equation:  $k_{inact} = \ln 2/t_{1/2}$ . <sup>f</sup> The kinetic results for compounds 4 (FCP), 8, 9, and vigabatrin were taken from reference [14]. <sup>g</sup> The kinetic results for compound 5 were extracted from reference [13]. <sup>h</sup> The kinetic results for compound 7 were taken from reference [15].

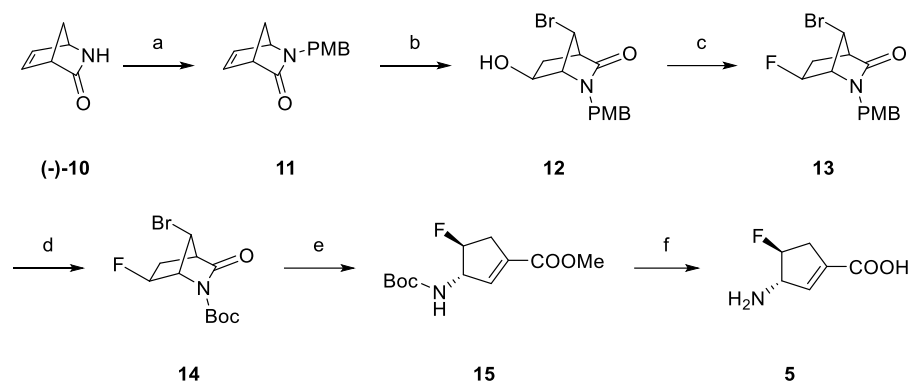
## 2. Results and Discussion

### 2.1. Synthesis of Monofluorinated Cyclopentene Analogs 5 and 6

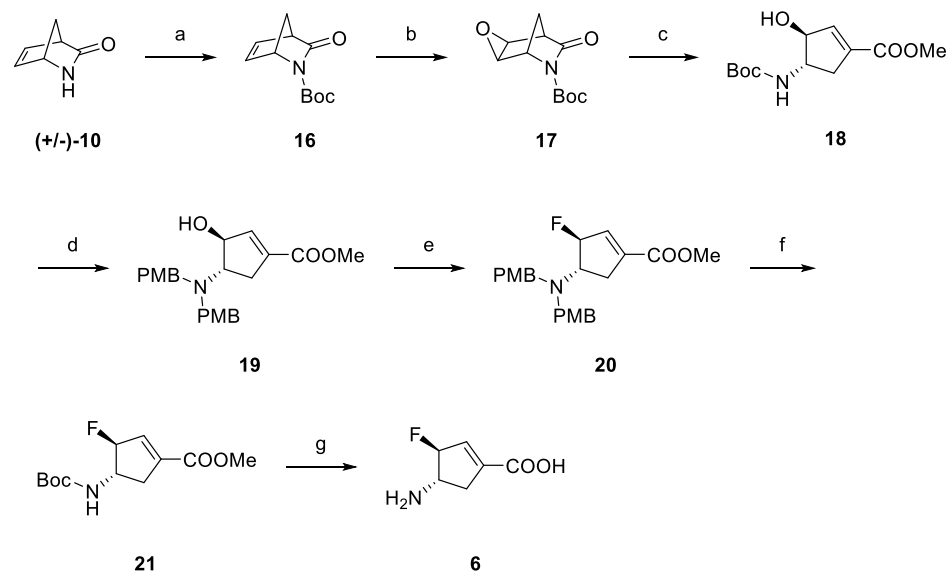
In the 10-step synthetic route that we previously reported for the preparation of 5 [13], an acid-assisted epoxide ring-opening reaction was utilized to form a bicyclic key intermediate containing a hydroxyl group on the bridgehead. The hydroxyl group was tosylated and employed as a leaving group to afford the desired cyclopentene ring through a one-pot lactam hydrolysis and  $\beta$ -elimination. To better support our mechanistic studies, in this work, we first optimized the preparation of 5 to a 6-step synthetic route (Scheme 4). Bicyclic lactam intermediate 12, bearing a bromo group on the bridgehead, was prepared from a chirally pure Vince lactam ((*S*)-10; (1*R*)-(−)-2-azabicyclo[2.2.1]hept-5-en-3-one; CAS#: 79200-56-9) following the procedure reported previously [22]. The hydroxyl-bearing carbon of 12 was fluorinated using DAST to generate 13 as a single diastereomer [13]. After switching the protecting group of the lactam from a PMB group to a Boc group (14), the lactam was hydrolyzed with  $K_2CO_3$ /MeOH. Simultaneously, the bromo group on the bridgehead of 14 was applied as a leaving group to induce  $\beta$ -elimination, forming the desired cyclopentene ring with the  $\alpha,\beta$ -unsaturated carboxylate methyl ester (15). The Boc group and methyl ester of 15 were removed with HCl/AcOH to afford the final product (5) as an HCl salt.

To prepare monofluorinated cyclopentene analog 6 bearing an  $\alpha,\epsilon$ -unsaturated carboxylate (Scheme 5), racemic Vince lactam (( $\pm$ )-10; ( $\pm$ )-2-azabicyclo[2.2.1]hept-5-en-3-one; CAS#: 49805-30-3) was first protected with a Boc group and then epoxidized using

*m*-CPBA (**17**) [13]. Intermediate **17** underwent a one-pot epoxide ring-opening, elimination, and lactam hydrolysis with  $K_2CO_3/MeOH$  [23,24], affording cyclopentene **18** an allylic alcohol. The Boc group of **18** was converted into a di-PMB protecting group (**19**) followed by fluorination using Deoxo-Fluor and then PMB/Boc group deprotection and methyl ester hydrolysis to give the final product (**6**) as an HCl salt. The kinetic constants shown in Table 1 indicate that only **6** shows reversible inhibition of GABA-AT ( $K_i = 0.14$  mM), and no inhibition was observed with *h*OAT up to 10 mM.



**Scheme 4.** The optimized synthetic route to compound **5**. Reagents and conditions. (a) (i) *p*-anisyl alcohol, conc. HCl, rt; (ii) NaH, TBAI, THF/DMF (10:1), 0 °C–rt; (b) (i) DBDMH, AcOH, 23 °C; (ii)  $K_2CO_3$ , MeOH 1 h; (c) DAST, DCM, –78 °C–rt; (d) (i) ceric ammonium nitrate,  $CH_3CN/H_2O$ , rt; (ii)  $Boc_2O$ , DIPEA, DMAP, DCM, rt; (e)  $K_2CO_3$ , MeOH, rt; (f) 4 N HCl, AcOH, 70 °C.



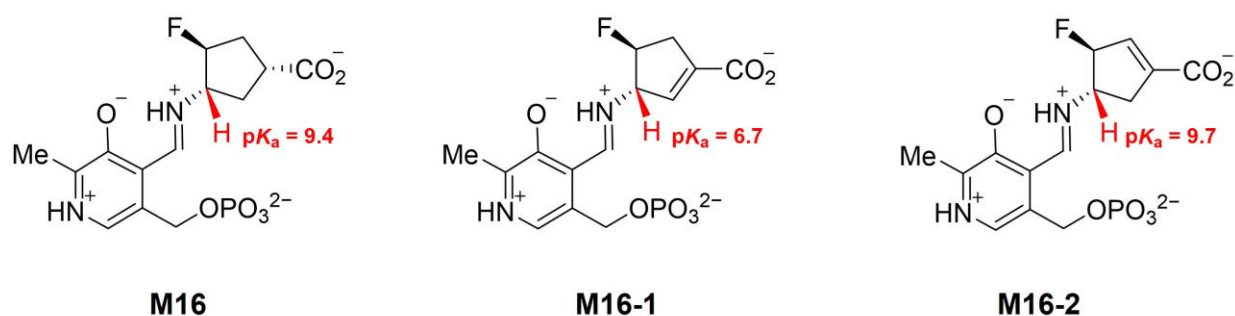
**Scheme 5.** The synthetic route to compound **6**. Reagents and conditions. (a)  $Boc_2O$ , DMAP (cat.), TEA, THF, rt; (b) *m*-CPBA, DCM, rt; (c)  $K_2CO_3$ , MeOH, rt; (d) (i) HCl (3M in MeOH), MeOH, rt; (ii) TEA, 4-anisaldehyde, DCE, rt; (iii) AcOH, DCE, 75 °C; (iv)  $NaBH(OAc)_3$ , DCE, 75 °C; (e) Deoxo-Fluor, DCM, –78 °C–rt; (f) (i) ceric ammonium nitrate,  $CH_3CN/H_2O$ , 0 °C–rt; (ii)  $Boc_2O$ , MeOH, rt; (g) 4N HCl, AcOH, 70 °C.

## 2.2. The Significance of the Conjugated Alkene of **5**

The deprotonation step (e.g., **M16** to **M17** in Scheme 3) is considered to be the rate-limiting step for enamine mechanism-based GABA-AT inactivators [3]. Previously, we used quantum mechanical cluster calculations on the deprotonation step, catalyzed by Lys329 in GABA-AT, to demonstrate that the ligand-PLP Schiff base **M16-1** (Figure 2A) [13], containing the added double bond, displays about 3 kcal/mol lower transition state (TS) energy compared with intermediate **M16**. In this work, we performed theoretical  $pK_a$

calculations using the DFT/B3LYP level of theory that we previously published [14,25,26] at 298K to predict the acidity at the  $C_\gamma$  position of difluoro analogs 4–6 (Table 1). The results, shown in Figure 2A, suggest that the hydrogen (highlighted in red) of PLP-bound 5 (**M16-1**) with an  $\alpha$ ,  $\beta$ -unsaturated carboxylate system displays the lowest  $pK_a$  value among the three analogs, while the  $pK_a$  value of the corresponding proton in PLP-bound 6 (**M16-2**) is not noticeably affected by the introduction of the double bond at the  $C_\alpha$  and  $C_\epsilon$  positions relative to parent cyclopentane 4 (**M16**). Electrostatic potential (ESP) calculations [14] (Figure 2B) indicate that the nucleophilicity of  $C_\delta$  in the enamine intermediate of 5 (**M19-1**) is much higher than that in the corresponding enamines of 4 and 6 (**M19** for 4 and **M19-2** for 6), suggesting that the  $C_\delta$  position of **M19-1** is more reactive than that in the other two intermediates, leading to more efficient enamine addition. In contrast, the enamine intermediate of 6 (**M19-2**) exhibits the lowest nucleophilicity, which should retard the attack at the internal aldimine, resulting in the modest inhibition of 6 on *hOAT*.

### A. $pK_a$ calculation DFT (B3LYP)



### B. Electrostatic potential calculations

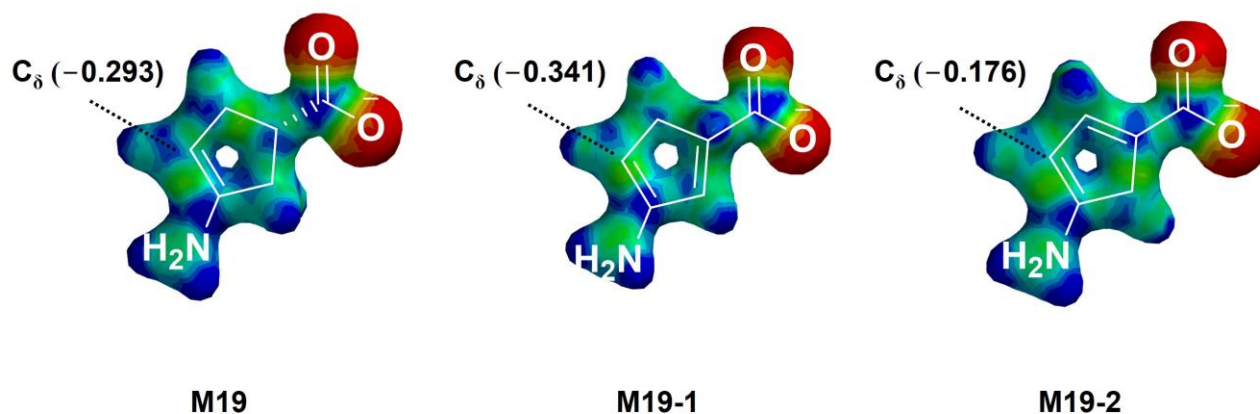


**Figure 2.** Theoretical  $pK_a$  calculations of the hydrogen at the  $C_\gamma$  position using (A) the DFT/B3LYP method and (B) electron density maps, color-coded according to the electrostatic potential (ESP) of intermediates and ESP charges at the  $C_\delta$  positions.

#### 2.3. The Unusual Covalent and Noncovalent Interactions between *hOAT* and the Products Generated from 5

Three different enamine mechanism-based inactivators—4, 5, and 8—were used to fully inactivate *hOAT*, and these samples were utilized in denaturing the intact protein MS [14] to evaluate the covalent inactivation adducts formed for these three compounds.



All the covalent mass shifts match the ketone adduct generated from the enamine addition pathway (Figure 3). Intriguingly, the major mass peaks are the modified peaks in the *h*OAT samples inactivated by **4** and **8** (Figure 3, left and right). In contrast, the apo-*h*OAT peak is the primary one in the sample treated with **5**, while only a small portion of *h*OAT was covalently modified by **5** (Figure 3, middle). According to our prior experience [26], these differences indicate that, unlike **4** and **8**, that noncovalent interaction is the predominant inactivation form in the case of **5**.

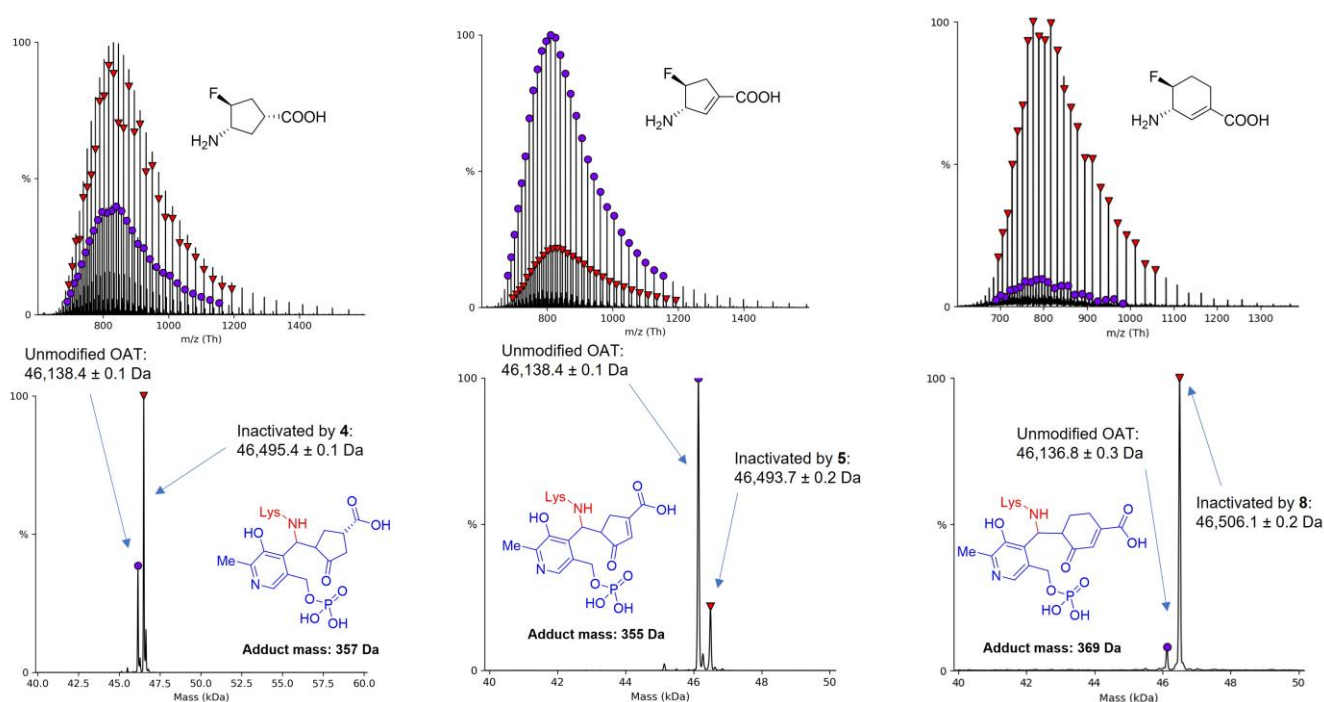


**Figure 3.** Denaturing intact protein mass spectrometry of *h*OAT inactivated by **4**, **5**, and **8**.

The subsequent wavelength absorbance measurement for **4**, **5**, and **8** after a 4 h incubation with *h*OAT (Figure 4, right) suggests that the final products of **4** and **8** exhibit maximal absorption at about 330 nm. This is consistent with the theoretical wavelengths (320–330 nm) for the final product generated from the enamine addition (Figure 4, left). In contrast, the final product of **5** displays a distinct maximal absorption at 460 nm.

We further carried out co-crystallization experiments to explore the final product of **5** in *h*OAT. The *h*OAT crystals grew within three days and showed orthorhombic morphology, with the largest dimension of ~0.2 mm. Crystals were transferred to a cryo-protectant solution and flash-frozen in liquid nitrogen. The acquired crystals diffracted to a resolution of 1.91 Å (Table S1). The crystal structure was solved using molecular replacement. The most well refined molecular model had three monomers in an asymmetric unit in the C121 space group. The overall protein fold of the monomer is a typical representative of a subgroup 2 aminotransferase [27]. Each monomer consists of an N-terminal domain that contains a loop, a helix, and a three-stranded  $\beta$ -meander, a small C-terminal domain that is most distant to the 2-fold axis, and a large domain that contributes most to the interface of the subunit. In an asymmetric unit, the monomers are related to each other by a 3-fold screw axis (Figure S2). Additionally, for each monomer, the active site is located at the interface of the subunit and the domain. The biological assembly of *h*OAT is a homodimer (Figure S3).

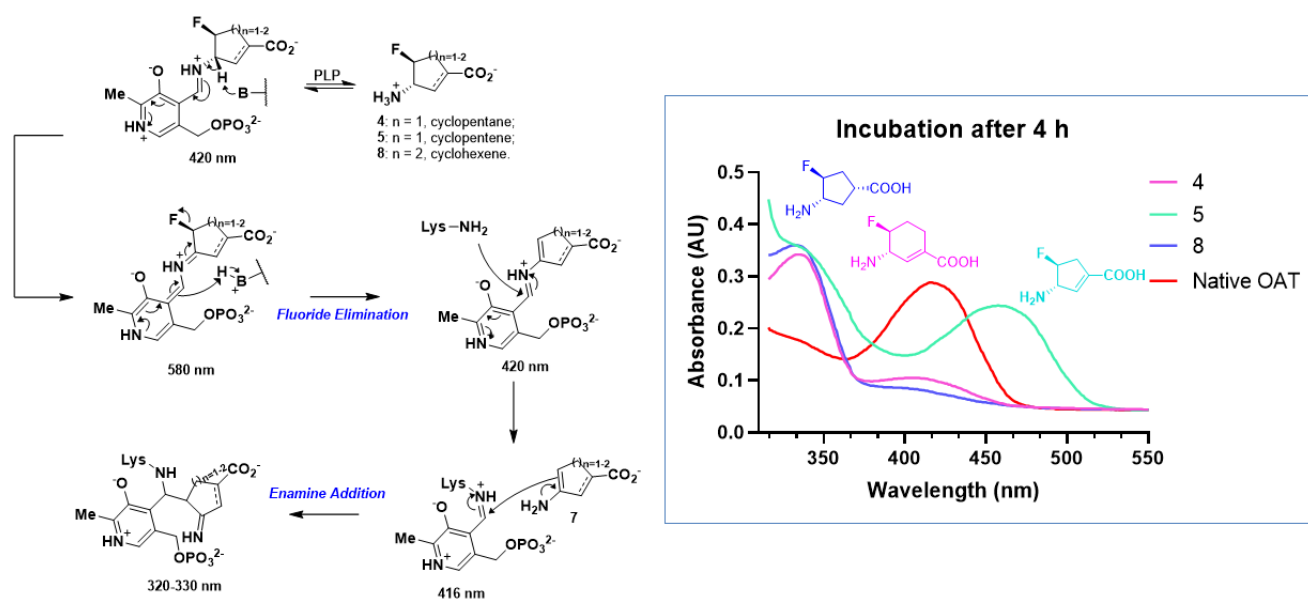


**Figure 4.** Wavelength absorbance measurement for **4**, **5**, and **8** after 4 h incubation with *h*OAT.

In the crystal structures of *h*OAT, inactivated by **4** (PDB code: 5VWO) and **8** (PDB code: 6V8D) [14,18], both compounds are covalently bonded to PLP, while their carboxylates interact with Tyr55 or Arg180. The structures of the *h*OAT-5 co-crystal (PDB code: 8EZ1), shown in Figure 5, suggest covalent modification of Lys292 by the ligand in one of the three protein copies as a minor form (Figure 5, left) and a noncovalent form of the ligand in the two other protein copies (Figure 5, right) as a major form. The conjugated structure of the noncovalent form explains the maximum absorbance at 460 nm. It should also be noted that the carboxylate group forms salt bridges with Arg413 and hydrogen bonds with Gln266 rather than interacting with Arg180 or Tyr55. Arg413 is known to form a salt bridge with Glu235 in the native enzyme [27], and this interaction was found to be preserved in most of the *h*OAT inactivators, such as the complexes with **4** and **8**. In the case of noncovalent inhibition by **5**, the ligand is located 2.8 Å away from Lys292, resulting in the additional translational freedom for the carboxylate group to anchor with Arg413. The unique binding orientation of **5** also led to a water-mediated hydrogen bond interaction between the imine group of the ligand and Tyr55 residue.

Compound **5** has a unique combination of structural and mechanistic features that differentiate it from previous inactivators. These unique features result in the disruption of the Arg413-Glu235 salt bridge, which has been observed with *h*OAT inactivated by another MBI, **22** (Figure 6) [28]. However, structurally, **22** is longer and bulkier compared to known *h*OAT ligands. **22** occupies the majority of the active site and forms hydrogen bonds with Tyr55, Arg413, and Gln266. In contrast, **5** is one of the smallest known *h*OAT inactivators, but its distinguishable inactivation mechanism allows it to orient itself in the active site in a way that it can also disrupt the Arg413-Glu235 salt bridge.

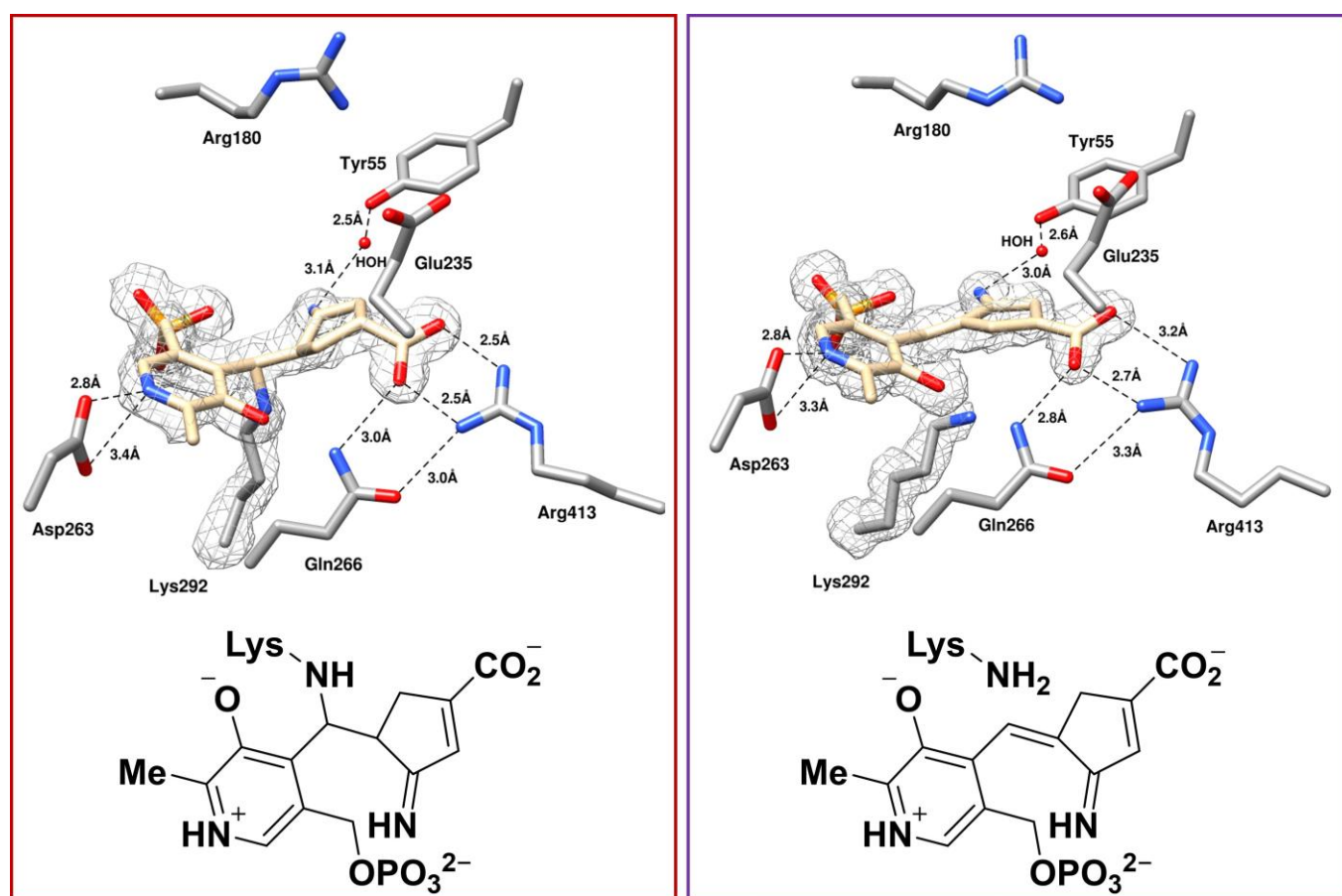


**Figure 5.** Co-crystal structure of *hOAT*, inactivated by **5**, representing two different ligand forms: covalent (**left**) and noncovalent (**right**) (PDB code: 8EZ1). Both forms were observed within the same co-crystal structure. The covalent form (referred to as minor) was observed in one of three protein copies, while the noncovalent form (referred to as major) was observed in the other two copies. The potential hydrogen bonds are shown as black dashed lines. For both ligand forms, composite omit ( $2F_o - F_c$ ) maps are shown at  $1.2\sigma$ . The occupancy factor for the ligand in all copies is equal to 1.0.

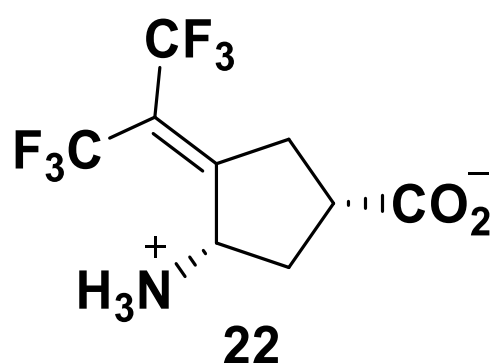
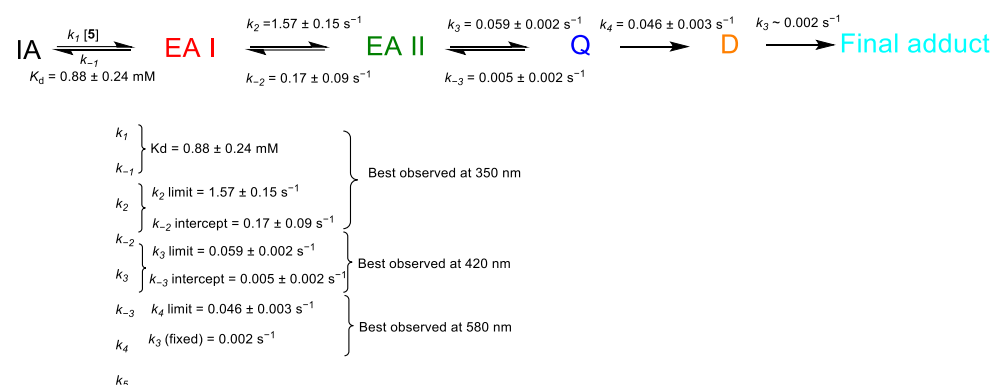


**Figure 6.** The structure of compound **22**.

#### 2.4. Transient-State Kinetics of *hOAT* Inactivation by **5**

Due to the uniqueness of compound **5**, transient-state spectrophotometric measurements were performed to observe the kinetics of the inhibition of *hOAT* by **5** (Scheme 6). Concentration dependences of the observed rate constants for individual phases were evaluated at 350, 420, and 580 nm. These wavelengths report principally on aldimine and quinonoid species. The data extracted at each wavelength were fit to Equation (4) in the experimental section that describes three exponential phases. At 350

nm, the observed rate constant for the first phase titrated hyperbolically to a limit. This indicates a rapid prior equilibrium for the association of **5** to form the first external aldimine species. The limiting rate constant for the forward decay of the external aldimine was  $1.57 \pm 0.15 \text{ s}^{-1}$  and the fit to Equation (5) that describes a hyperbolic dependence with a positive y-intercept that defines the rate constant for the reverse reaction. This fit gave the dissociation constant ( $k_{-1}/k_1$ ) for **5** to the *h*OAT internal aldimine of  $1.44 \pm 0.60 \text{ mM}$  and a value for the rate constant for the decay of the external aldimine to the internal aldimine ( $k_{-2}$ ) of  $0.17 \pm 0.09 \text{ s}^{-1}$  (Figure 7A).



**Scheme 6.** The rate constants for the observed transient states during the inhibition of *h*OAT by **5**.

The data extracted for 420 nm were fit by fixing the first phase to the  $k_{\text{obs}}$  values determined for the first phase at 350 nm, where the first phase is well-delineated from the second. The second phase observed represents the decay of a second external aldimine-like species (see below) into a quinonoid with maximal absorption at 580 nm. The concentration dependence of the observed rate constant for the second phase gave a hyperbolic shape, indicating the reversibility of the prior step ( $k_2$  and  $k_{-2}$  in Scheme 6). These data also fit best to Equation (5), and the limit of this dependence revealed a limiting forward rate constant ( $k_3$ ) of  $0.059 \pm 0.002 \text{ s}^{-1}$  for the formation of the quinonoid intermediate. For the reverse reaction ( $k_{-3}$ ), the rate constant was  $0.005 \pm 0.002 \text{ s}^{-1}$ , Figure 7B). The data extracted for 580 nm report the formation and decay of the quinonoid and the decay of the subsequent diamine-like species (Figure 7). These data were fit by fixing the rate constant value for the final phase that represents the apparently irreversible decay of the diamine-like species to  $0.002 \text{ s}^{-1}$  ( $k_5$ ). This was done in part because the endpoint of the final phase was not definitively captured at the limit of the data collection (1250 s), and so no measure of error was obtained for the rate constant of this step. The fit reveals that the dependence is again hyperbolic due to the reversibility of the preceding step ( $k_3$ ,  $k_{-3}$ ), that it has a net rate constant ( $k_4$ ) of  $0.046 \pm 0.003 \text{ s}^{-1}$  with no evidence for reversibility and was fit to Equation (6). Scheme 6 depicts the summation of these observations.

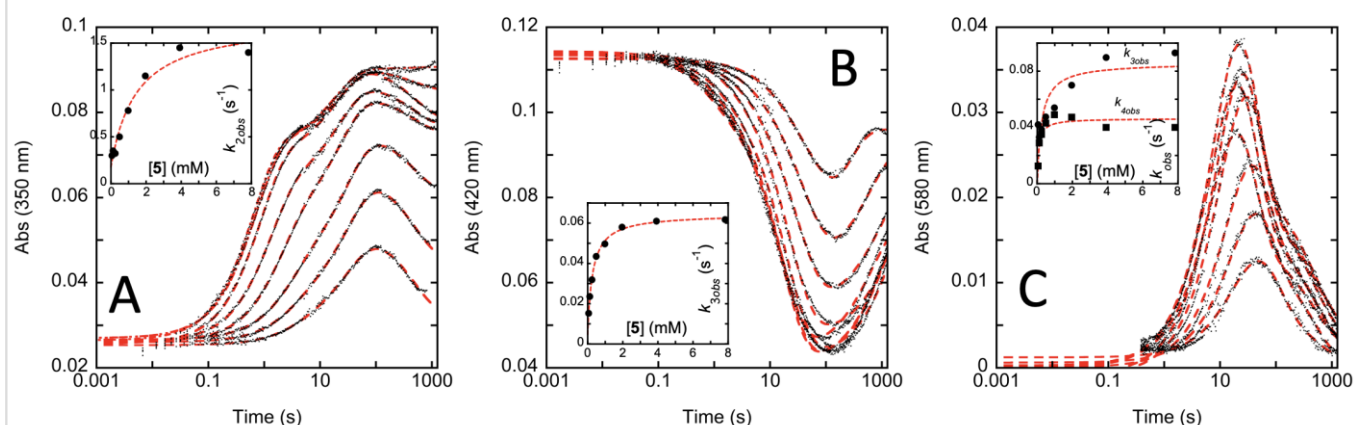


**Figure 7.** Single-wavelength analytical evaluation of the rate constants observed for *h*OAT reaction with inactivator **5**. *h*OAT (13.4  $\mu$ M) was allowed to react with varied concentrations of compound **5** (62, 123, 245, 490, 980, 1960, 3920 and 7830  $\mu$ M) at pH 7.5 at 10  $^{\circ}$ C (all concentration indicated are post-mixing). Reaction traces at specific wavelengths of 350, 420, and 580 nm were extracted from the spectral data and combined into nested datasets that depict the concentration dependence of the processes observed. (A) The concentration dependence of the data collected at 350 nm, was fit to Equation (4). Concentrations increase for successive ascending traces. The inset is the dependence of the first observed phase, assigned as reporting on the  $k_2$ ,  $k_{-2}$  step in Scheme 6. The dependence was fit to Equation (5). (B) Concentration dependence of the data, collected at 420 nm, was fit to Equation (4). In this fit, the values of the rate constants for the first phase were fixed to the values determined in A. Concentrations decrease for successive ascending traces. Inset is the dependence of the second observed phase, assigned as reporting on the  $k_3$ ,  $k_{-3}$  step in Scheme 6. The dependence was fit to Equation (5). (C) Concentration dependence of the data collected at 580 nm was fit to Equation (4). In this fitting, the values of the rate constants for the third phase that was assigned to  $k_5$  in Scheme 6 were fixed to 0.002  $s^{-1}$  as an approximate measure of this process. Concentrations increase for successive ascending traces for the first six concentrations, and then the traces decrease in total amplitude for the highest two concentrations. Inset is the dependence of the first and second observed phases, assigned as reporting on the  $k_3$ ,  $k_{-3}$ , and  $k_4$  steps in Scheme 6, respectively. The  $k_{3obs}$  dependence was fit to Equation (5), and the  $k_{4obs}$  dependence was fit to Equation (6).

Spliced charge-coupled device (CCD) datasets were fit using singular value decomposition (SVD) to deconvolute the data, yielding spectra for all species observed. The dataset obtained for 1960  $\mu$ M of **5** was used to avoid complexity associated with enzyme precipitation at higher concentrations. The dataset fits best to an irreversible four-step model, consistent with data for a single-compound concentration that by themselves contain no evidence of reversibility. The rate constants obtained from the fit were as follows:  $k_2 = 1.22 \pm 0.02$ ,  $k_3 = 0.11 \pm 0.01$ ,  $k_4 = 0.014 \pm 0.01$ ,  $k_5 = 0.0023 \pm 0.0002$  (numbered according to Scheme 6) (Figure 7). These rate constants are consistent with the values determined from analytical fits to exponentials at this concentration of inhibitor. In Figure 8, the time-zero spectrum for the *h*OAT internal aldimine was included for reference and but was not observed in the data. The time-zero spectrum was obtained by mixing *h*OAT with buffer (black dashed spectrum). The spectrum of the first species observed is consistent with that of an external aldimine (red spectrum). This species decays into a broader aldimine-like spectrum (green spectrum) before decaying to form a definitive quinonoid species (blue spectrum). The quinonoid decays to form a species largely devoid of visible wavelength absorption that is presumably a less conjugated diamine species (yellow spectrum). This species then decays to produce a third aldimine-like spectrum (cyan spectrum).



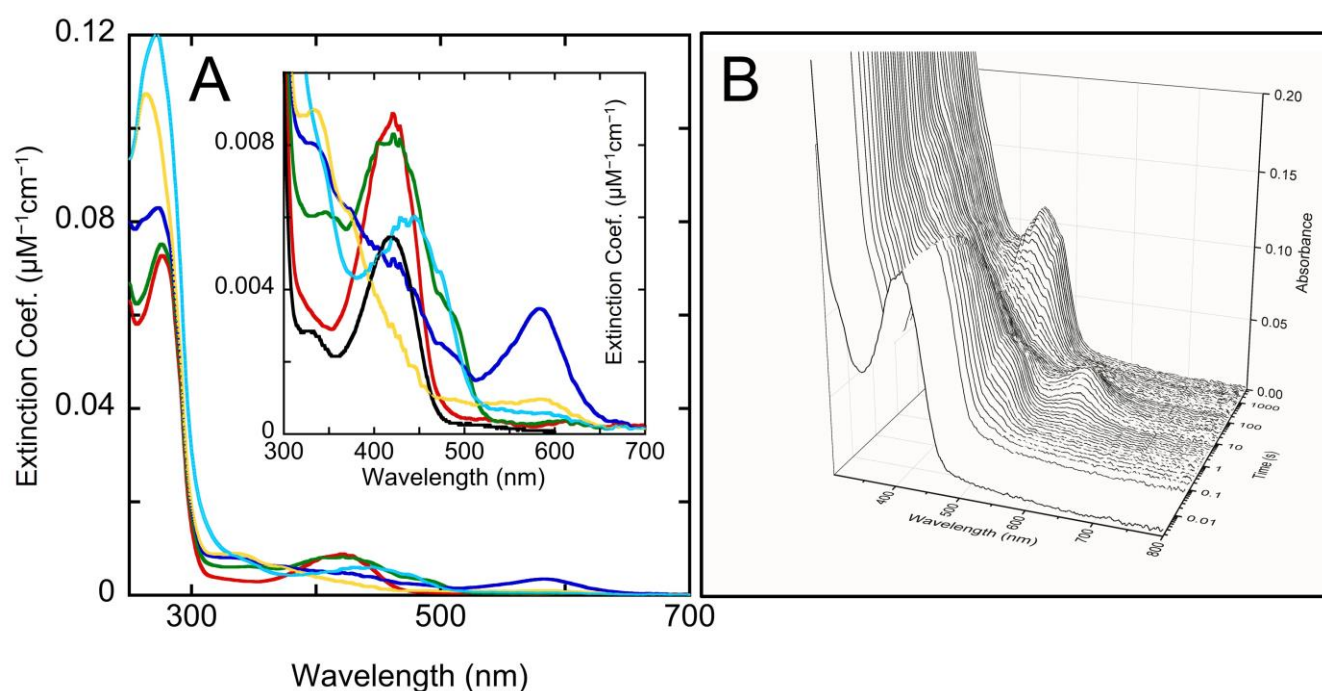
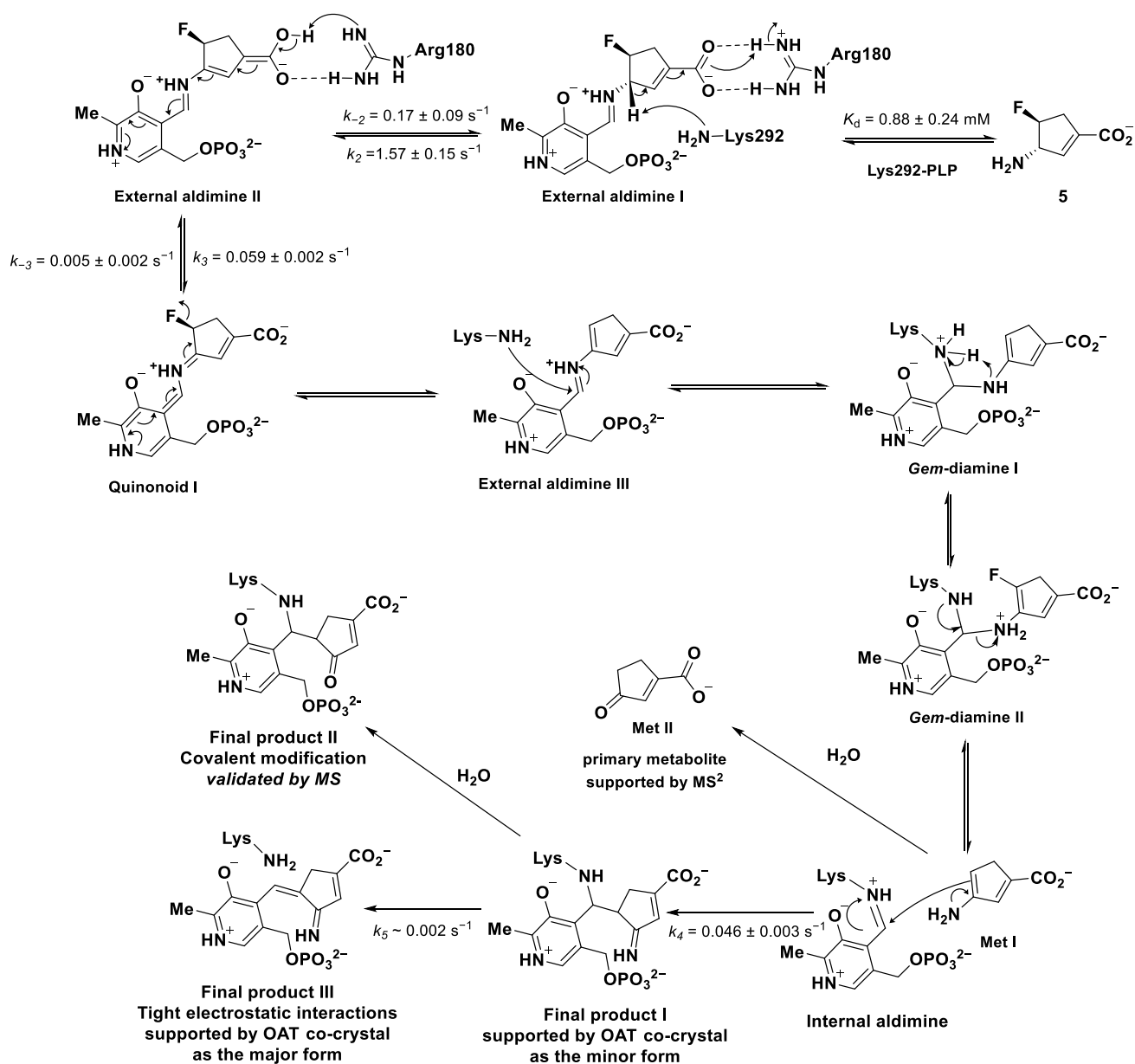


**Figure 8.** Spectral deconvolution of transient-state CCD data. *hOAT* (13.4  $\mu\text{M}$ ) was allowed to react with 1960  $\mu\text{M}$  of **5** at pH 7.5 at 10  $^{\circ}\text{C}$  (all concentrations indicated are post-mixing). **(A)** Spectra derived from singular value decomposition spectral deconvolution. The spectra arise in the following order, red, green, blue, yellow, cyan. Inset depicts the region of the spectrum from 300–700 nm. In this plot, the time-zero spectrum of the *hOAT* internal aldimine is added for reference (black spectrum). **(B)** Three-dimensional depiction of the absorption changes of the *hOAT*-**5** inhibition reaction.

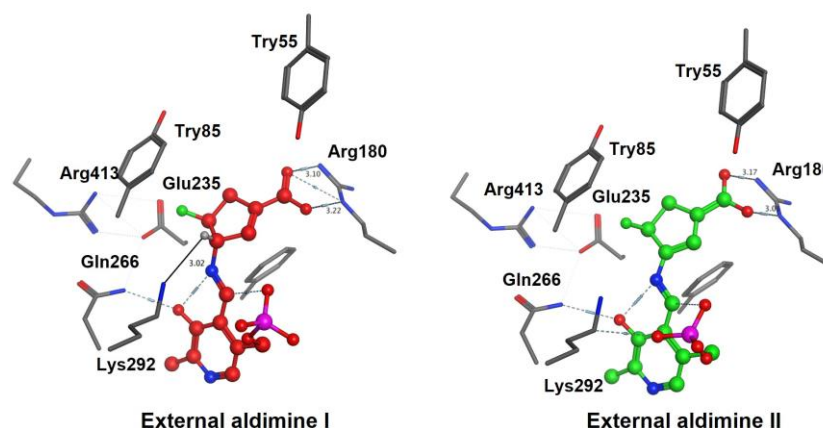
### 2.5. The Inactivation Pathway of Compound **5** in *hOAT*

It should be noted that, in general, a quinonoid species ( $\sim 580$  nm) is thought to be formed right after the first external aldimine ( $\sim 420$  nm) (Figure 4, left). However, the transient-state measurement suggests that there is an additional broad aldimine-like species (green spectrum, Figure 8) observed between the quinonoid and the first external aldimine. We thus speculated that **External Aldimine I** (shown in Scheme 7) may generate an enolate structure as **External Aldimine II**, which establishes dual interactions with Arg180 based on the molecular docking studies shown in Figure 9A. Free energy calculations in Figure 9B also support the existence of **External Aldimine II** tautomers, showing comparable results with **External Aldimine I**. Subsequently, **External Aldimine II** can undergo further tautomerization, triggered by the lone pair of electrons on Arg180, to form **Quinonoid I**. The elimination of the fluoride ion gives **External Aldimine III**, which can undergo attack by Lys292. This transient state further goes through the states of **gem-Diamines I and II** and releases enamine intermediate **Met I**. By mass spectrometry analysis, ketone intermediate **Met II** was detected as the predominant metabolite generated after incubating **5** with *hOAT*, validating the formation of **Met I** (Figure S1). The nucleophilic enamine intermediate **Met I** efficiently attacks the PLP-Lys292 **Internal Aldimine** and produces **Final Product I**, thereby inactivating the enzyme, which is covalently bound to PLP. Hydrolysis of the imine of **Final Product I** gives **Final Product II**. Elimination of Lys292 leads to **Final Product III** as the major form, which is in equilibrium with **Final Product I** (the minor form).



Scheme 7. Possible inactivation mechanisms of 5 with hOAT.

### A. Docking poses



### B. Free energy calculations

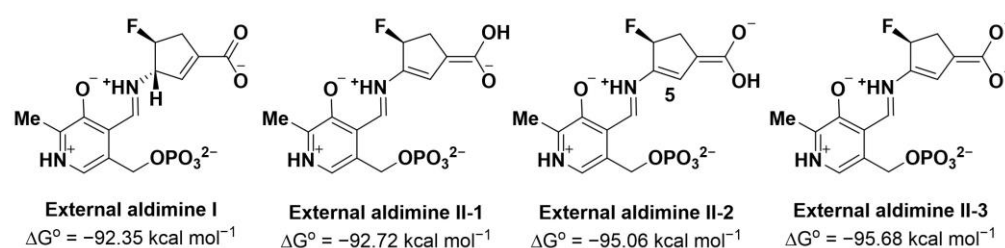


**Figure 9.** (A) Molecular docking poses and (B) free energy calculations of potential external aldimines I and II.

## 3. Materials and Methods

### 3.1. Chemistry

**General Procedure.** Commercially available reagents and solvents were used without further purification. All reactions were monitored by thin-layer chromatography (TLC) using 0.25 mm SiliCycle extra-hard 250  $\mu$ m TLC plates (60 F254), and spots were visualized under UV (254 nm) and ceric ammonium molybdate or ninhydrin staining. Flash chromatography was performed on a Combi-Flash Rf system (Teledyne ISCO) with silica columns and reverse-phase C-18 columns. Analytical HPLC was used to determine the purity of all the final products using an Agilent 1260 series instrument with the following conditions: column, Phenomenex Kintex C-18 column (50  $\times$  2.1 mm, 2.6  $\mu$ m); mobile phase, 5–100% acetonitrile/water containing 0.05% TFA at a flow rate of 0.9 mL/min for 6 min; UV detection at 254 nm. <sup>1</sup>H and <sup>13</sup>C NMR spectra were obtained using the Bruker AVANCE III 500 MHz system and Bruker NEO console w/QCI-F cryoprobe 600 MHz system. Chemical shifts were reported relative to CDCl<sub>3</sub> ( $\delta$  = 7.26 for <sup>1</sup>H NMR and  $\delta$  = 77.16 for <sup>13</sup>C NMR spectra) and CD<sub>3</sub>OD ( $\delta$  = 3.31 for <sup>1</sup>H NMR and  $\delta$  = 49.15 for <sup>13</sup>C NMR spectra). The following abbreviations for multiplicities were used: s = singlet; d = doublet; t = triplet; q = quartet; m = multiplet; dd = doublet of doublets; dt = doublet of triplets; dq = doublet of quartets, ddt = doublet of doublet of triplets, ddd = doublet of doublet of doublets; dddd = doublet of doublet of doublet of doublets; dddd = doublet of doublet of doublet of triplets; br s = broad singlet. Low-resolution mass spectra (LRMS) were obtained using a Thermo TSQ Quantum system in the positive ion mode using atmospheric pressure chemical ionization (APCI)/electrospray ionization (ESI) with a reverse-phase Agilent Infinity 1260 HPLC system. High-resolution mass spectra (HRMS) were obtained on an Agilent 6210 LC-TOF spectrometer in the positive ion mode using electrospray ionization (ESI) with an Agilent G1312A HPLC pump and an Agilent G1367B autoinjector at the Integrated Molecular Structure Education and Research Center



(IMSERC), Northwestern University. The purity of all tested compounds for in vitro biological studies was >95%, assessed by HPLC analysis.

**(1R,4R,6S,7R)-7-Bromo-6-hydroxy-2-(4-methoxybenzyl)-2-azabicyclo[2.2.1]heptan-3-one (12)** was synthesized from (1R)-(-)-2-azabicyclo[2.2.1]hept-5-en-3-one ((-)-10, CAS#: 79200-56-9, 30 g, 270 mmol) following the procedure published previously [29]. The desired product **12** was afforded as an off-white solid (27.3 g, 31% over two steps). <sup>1</sup>H NMR (500 MHz, CDCl<sub>3</sub>) δ 7.19–7.12 (m, 2H), 6.92–6.85 (m, 2H), 4.58 (d, *J* = 14.7 Hz, 1H), 4.24 (t, *J* = 1.7 Hz, 1H), 3.98 (d, *J* = 14.7 Hz, 1H), 3.96–3.92 (m, 1H), 3.71 (s, 1H), 2.95 (dd, *J* = 3.8, 1.9 Hz, 1H), 2.49–2.37 (m, 2H), 2.15 (dt, *J* = 13.8, 3.8 Hz, 1H). <sup>13</sup>C NMR (126 MHz, CDCl<sub>3</sub>) δ 172.6, 159.6, 129.7 (2C), 128.0, 114.6 (2C), 65.7, 55.5, 50.8, 50.5, 44.1, 33.7. LRMS (APCI) calc. for C<sub>14</sub>H<sub>17</sub>BrNO<sub>3</sub> [M+H]<sup>+</sup>: 326.04; found, 326.21; T<sub>R</sub> = 2.00 min.

**(1R,4R,6S,7R)-7-Bromo-6-fluoro-2-(4-methoxybenzyl)-2-azabicyclo[2.2.1]heptan-3-one (13)**. To a stirred solution of **12** (1000 mg, 3.07 mmol) in DCM (20 mL) was added DAST (0.41 mL, 4.60 mmol) at 0 °C. The resulting mixture was slowly warmed to room temperature and stirred overnight. After the completion of the reaction, the solution was quenched with water and extracted with DCM (30 mL × 3). The combined organic layers were separated, washed with brine, dried over Na<sub>2</sub>SO<sub>4</sub>, and concentrated under vacuum conditions. The crude product was purified via Combi-Flash chromatography (EtOAc/hexane: 0–100%) to yield **13** as a colorless oil (900 mg, 90%). <sup>1</sup>H NMR (500 MHz, CDCl<sub>3</sub>) δ 7.16 (d, *J* = 8.3 Hz, 2H), 6.89 (d, *J* = 8.4 Hz, 2H), 4.64 (dddd, *J* = 53.8, 7.3, 2.8, 1.4 Hz, 1H), 4.49 (d, *J* = 14.7 Hz, 1H), 4.21 (s, 1H), 4.07 (d, *J* = 14.7 Hz, 1H), 3.90 (s, 1H), 3.82 (s, 3H), 2.97–2.88 (m, 1H), 2.45 (ddt, *J* = 27.8, 13.9, 3.5 Hz, 1H), 2.36–2.25 (m, 1H). <sup>13</sup>C NMR (126 MHz, CDCl<sub>3</sub>) δ 172.9, 159.7, 129.8 (2C), 127.8, 114.7 (2C), 90.77 (d, *J* = 200.1 Hz), 64.50 (d, *J* = 22.8 Hz), 55.5, 50.52 (d, *J* = 2.4 Hz), 48.05 (d, *J* = 1.9 Hz), 44.4, 31.10 (d, *J* = 21.6 Hz). LRMS (APCI) calc. for C<sub>14</sub>H<sub>16</sub>BrFNO<sub>2</sub> [M+H]<sup>+</sup>: 328.03; found, 328.10; T<sub>R</sub> = 2.62 min.

**(1R,4R,6S,7R)-tert-Butyl 7-Bromo-6-fluoro-3-oxo-2-azabicyclo[2.2.1]heptane-2-carboxylate (14)**. (i) To a stirred solution of **13** (900 mg, 2.75 mmol) in CH<sub>3</sub>CN (40 mL) was added an aqueous solution of ceric ammonium nitrate (4.52 g in 12 mL water, 8.26 mmol) at room temperature. The resulting mixture was stirred for 2 h until the starting material disappeared. After the completion of the reaction, the reaction mixture was concentrated under vacuum conditions, and the residue was extracted with EtOAc (25 mL × 3). The combined organic layers were separated, washed with sat. Na<sub>2</sub>CO<sub>3</sub> solution and brine, dried over Na<sub>2</sub>SO<sub>4</sub>, and concentrated under vacuum conditions. The crude product was purified via Combi-Flash chromatography (EtOAc-hexane: 0–100%) to lactam intermediate (330 mg, 1.60 mmol) as an off-white solid. (ii) To a stirred solution of lactam intermediate (330 mg, 1.60 mmol) in DCM (20 mL) were added DIPEA (0.33 mL, 1.91 mmol), DMAP (20 mg, 0.16 mmol), and Boc<sub>2</sub>O (381 mg, 1.75 mmol) at room temperature, and the resulting mixture was stirred at room temperature for 3 h. After the completion of the reaction, the solution was quenched with sat. NH<sub>4</sub>Cl solution and extracted with DCM (25 mL × 3). The combined organic layers were separated, washed with brine, dried over Na<sub>2</sub>SO<sub>4</sub>, and concentrated under vacuum conditions. The crude product was purified via Combi-Flash chromatography (EtOAc/Hexane: 0–60%) to yield **14** (480 mg, 56% over two steps) as a white solid. <sup>1</sup>H NMR (500 MHz, CDCl<sub>3</sub>) δ 4.95 (dddd, *J* = 52.9, 5.9, 3.1, 1.6 Hz, 1H), 4.75 (s, 1H), 4.32 (t, *J* = 1.6 Hz, 1H), 3.00 (dt, *J* = 4.0, 1.7 Hz, 1H), 2.54 (ddt, *J* = 28.3, 14.3, 3.6 Hz, 1H), 2.47–2.39 (m, 1H), 1.53 (s, 9H). <sup>13</sup>C NMR (126 MHz, CDCl<sub>3</sub>) δ 169.9, 147.8, 90.77 (d, *J* = 199.6 Hz), 84.8, 64.12 (d, *J* = 24.3 Hz), 51.82 (d, *J* = 2.5 Hz), 45.50 (d, *J* = 1.9 Hz), 30.84 (d, *J* = 22.0 Hz), 28.1 (3C). LRMS (APCI) calc. for C<sub>11</sub>H<sub>16</sub>BrFNO<sub>3</sub> [M+H]<sup>+</sup>: 308.03; found, 308.26; T<sub>R</sub> = 2.70 min.

**(3S,4S)-Methyl 3-((tert-Butoxycarbonyl)amino)-4-fluorocyclopent-1-enecarboxylate (15)**. To a stirred solution of **14** (480 mg, 1.56 mmol) in MeOH (20 mL) was added K<sub>2</sub>CO<sub>3</sub> (647 mg, 4.69 mmol) at room temperature. Then, the resulting mixture was stirred for an additional 1 h and then neutralized with sat. NH<sub>4</sub>Cl solution and extracted with EtOAc (25 mL × 3). The combined organic layers were separated, washed with brine, dried over Na<sub>2</sub>SO<sub>4</sub>, and concentrated under vacuum conditions. The crude product was purified

via Combi-Flash chromatography (EtOAc/Hexane: 0–60%) to yield **15** (190 mg, 47%) as a white solid.  $^1\text{H}$  NMR (500 MHz,  $\text{CDCl}_3$ )  $\delta$  6.58 (s, 1H), 5.20–4.98 (m, 1H), 4.80 (d,  $J$  = 21.3 Hz, 1H), 4.58 (s, 1H), 3.77 (s, 3H), 3.06 (dddt,  $J$  = 22.1, 18.0, 6.4, 1.9 Hz, 1H), 2.76 (dddt,  $J$  = 26.9, 17.9, 2.8, 1.3 Hz, 1H), 1.45 (s, 9H).  $^{13}\text{C}$  NMR (126 MHz,  $\text{CDCl}_3$ )  $\delta$  164.5, 154.9, 138.8, 136.5, 97.60 (d,  $J$  = 184.1 Hz), 80.51, 62.86 (d,  $J$  = 33.0 Hz), 52.1, 37.43 (d,  $J$  = 24.8 Hz), 28.5 (3C). LRMS (APCI) calc. for  $\text{C}_7\text{H}_{10}\text{FNO}_2$   $[\text{M}-\text{Boc}+\text{H}]^+$ : 159.07; found, 158.91;  $T_R$  = 2.56 min.

**(3S,4S)-3-Amino-4-fluorocyclopent-1-enecarboxylic acid hydrochloride (5).** To a stirred solution of **15** (190 mg, 0.73 mmol) in acetic acid (7 mL) was added 4N HCl (7 mL) at room temperature, and the resulting mixture was heated at 70 °C overnight. After the completion of the reaction, the excess solvent was removed under vacuum conditions. The crude product was washed with acetonitrile to afford **5** (130 mg, 98%) as an off-white solid.  $^1\text{H}$  NMR (500 MHz,  $\text{CD}_3\text{OD}$ )  $\delta$  6.55 (s, 1H), 5.33 (ddt,  $J$  = 51.0, 6.4, 3.0 Hz, 1H), 4.54 (dt,  $J$  = 22.1, 2.8, 1.5 Hz, 1H), 3.22 (dddt,  $J$  = 19.9, 18.4, 7.0, 2.0 Hz, 1H), 2.83 (dddt,  $J$  = 27.6, 18.3, 3.2, 1.5 Hz, 1H).  $^{13}\text{C}$  NMR (126 MHz, MeOD)  $\delta$  166.1, 142.1, 134.0, 95.99 (d,  $J$  = 183.6 Hz), 63.29 (d,  $J$  = 31.4 Hz), 38.75 (d,  $J$  = 24.5 Hz). HRMS (ESI) calc. for  $\text{C}_6\text{H}_9\text{FNO}_2$   $[\text{M}+\text{H}]^+$ : 146.0612; found, 146.0613.

**(±)-tert-Butyl 3-Oxo-2-azabicyclo[2.2.1]hept-5-ene-2-carboxylate (16).** To a stirred solution of (±)-2-azabicyclo[2.2.1]hept-5-en-3-one (**(±)-10**, CAS# 49805-30-3, 2.5 g, 23 mmol) in DCM (250 mL) were added Boc<sub>2</sub>O (6.0 g, 27.5 mmol), TEA (3.83 mL, 27.5 mmol), and DMAP (280 mg, 2.3 mmol). The resulting mixture was stirred at room temperature overnight. After the completion of the reaction, the solution was quenched with water and extracted with DCM (25 mL × 3). The combined organic layers were separated, washed with brine, dried over  $\text{Na}_2\text{SO}_4$ , and concentrated under vacuum conditions. The crude product was purified via Combi-Flash chromatography (EtOAc/hexane: 0–100%) to give **16** (4.5 g, 94%) as an off-white solid.  $^1\text{H}$  NMR (500 MHz,  $\text{CDCl}_3$ )  $\delta$  6.87 (dd,  $J$  = 5.3, 2.4 Hz, 1H), 6.64 (dq,  $J$  = 5.3, 1.6 Hz, 1H), 4.94 (s, 1H), 3.36 (s, 1H), 2.39–2.26 (m, 1H), 2.13 (dt,  $J$  = 8.5, 1.3 Hz, 1H), 1.48 (s, 9H).  $^{13}\text{C}$  NMR (126 MHz,  $\text{CDCl}_3$ )  $\delta$  176.3, 150.5, 140.1, 138.3, 82.7, 62.5, 55.0, 54.6, 28.2 (3C). LRMS (APCI) calc. for  $\text{C}_{11}\text{H}_{16}\text{NO}_3$   $[\text{M}+\text{H}]^+$ : 210.11; found, 209.93.

**(±)-tert-Butyl 7-Oxo-3-oxa-6-azatricyclo[3.2.1.0<sup>2,4</sup>]octane-6-carboxylate (17).** To a stirred solution of **16** (4.5 g, 21.5 mmol) in  $\text{CHCl}_3$  (150 mL) was added *m*-CPBA (7.2 g, ~77%, 32.3 mmol) at room temperature under an argon atmosphere. The resulting mixture was stirred at 65 °C overnight. After the completion of the reaction, the solution was quenched with sat.  $\text{Na}_2\text{S}_2\text{O}_3$  solution and extracted with  $\text{CHCl}_3$  (100 mL × 3). The combined organic layers were separated, washed with sat.  $\text{Na}_2\text{CO}_3$  solution and brine, dried over  $\text{Na}_2\text{SO}_4$ , and concentrated under vacuum conditions. The crude product was purified via Combi-Flash chromatography (EtOAc/hexane: 0–100%) to yield **17** (2.3 g, 48%) as an off-white solid.  $^1\text{H}$  NMR (500 MHz,  $\text{CDCl}_3$ )  $\delta$  4.61 (p,  $J$  = 1.6 Hz, 1H), 3.77 (dd,  $J$  = 3.6, 1.2 Hz, 1H), 3.61 (dd,  $J$  = 3.7, 1.5 Hz, 1H), 3.06 (p,  $J$  = 1.6 Hz, 1H), 1.81 (dt,  $J$  = 10.4, 1.7 Hz, 1H), 1.70–1.61 (m, 1H), 1.52 (s, 9H).  $^{13}\text{C}$  NMR (126 MHz,  $\text{CDCl}_3$ )  $\delta$  173.5, 149.9, 83.5, 59.1, 53.3, 50.1, 48.5, 28.2 (3C), 27.2. LRMS (APCI) calc. for  $\text{C}_{11}\text{H}_{16}\text{NO}_4$   $[\text{M}+\text{H}]^+$ : 226.11; found, 226.04.

**Methyl trans-4-((tert-Butoxycarbonyl)amino)-3-hydroxycyclopent-1-enecarboxylate (18).** To a stirred solution of **17** (1.0 g, 4.44 mmol) in MeOH (30 mL) was added  $\text{K}_2\text{CO}_3$  (1.84 g, 13.3 mmol). The resulting mixture was stirred at room temperature for 1 h. After the completion of the reaction, the solution was quenched with sat.  $\text{NH}_4\text{Cl}$  solution and extracted with DCM (25 mL × 3). The combined organic layers were separated, washed with sat.  $\text{Na}_2\text{CO}_3$  solution and brine, dried over  $\text{Na}_2\text{SO}_4$ , and concentrated under vacuum conditions. The crude product was purified via Combi-Flash chromatography (EtOAc/hexane: 0–100%) to yield **18** (0.9 g, 79%) as a white solid.  $^1\text{H}$  NMR (500 MHz,  $\text{DMSO}-d_6$ )  $\delta$  7.14 (d,  $J$  = 7.8 Hz, 1H), 6.50 (q,  $J$  = 1.9 Hz, 1H), 5.31 (d,  $J$  = 6.6 Hz, 1H), 4.59 (tq,  $J$  = 6.0, 2.0 Hz, 1H), 3.78 (p,  $J$  = 8.2, 7.2 Hz, 1H), 3.67 (s, 3H), 2.76 (dd,  $J$  = 16.1, 8.2 Hz, 1H), 2.21 (ddt,  $J$  = 16.2, 6.7, 2.1 Hz, 1H), 1.39 (s, 9H).  $^{13}\text{C}$  NMR (126 MHz,  $\text{DMSO}-d_6$ )  $\delta$  164.5, 155.3, 143.8, 133.6, 79.7, 77.7, 59.3, 51.5, 36.1, 28.2 (3C). LRMS (APCI) calc. for  $\text{C}_7\text{H}_{11}\text{NO}_3$   $[\text{M}-\text{Boc}+\text{H}]^+$ : 157.07; found, 157.59.

**Methyl *trans*-4-(Bis(4-methoxybenzyl)amino)-3-hydroxycyclopent-1-ene-1-carboxylate (19).** (i) To a stirred solution **18** (3.00 g, 11.7 mmol) in MeOH (15 mL) was added 3M HCl in MeOH (30 mL). The resulting mixture was stirred at room temperature under an argon atmosphere for 1 h. After the completion of the reaction, the excessive solution was removed under vacuum conditions. The crude product was used directly in the next step. (ii) To a stirred solution of the crude product (theoretically 2.257 g, 11.66 mmol) in DCE (72.9 mL) were added TEA (3.25 mL, 23.332 mmol) and 4-anisaldehyde (4.26 mL, 34.98 mmol). The resulting mixture was stirred under an argon atmosphere at room temperature until all the starting material was dissolved in solution, followed by the addition of AcOH (2.67 mL, 46.65 mmol). The resulting mixture was then stirred at 75 °C for an additional 1 h under an argon atmosphere. After that, the reaction solution was then cooled to room temperature, and NaBH(OAc)<sub>3</sub> (7.412 g, 34.98 mmol, 3.0 equiv) was slowly added to the solution. The resulting mixture was then stirred at 75 °C under an argon atmosphere overnight. After the completion of the reaction, the solution was quenched with sat. NH<sub>4</sub>Cl solution and extracted with DCM (25 mL × 3). The combined organic layers were separated, washed with sat. Na<sub>2</sub>CO<sub>3</sub> solution and brine, dried over Na<sub>2</sub>SO<sub>4</sub>, and concentrated under vacuum conditions. The crude product was purified via Combi-Flash chromatography (EtOAc/hexane: 0–100%) to yield **19** (2.7 g, 58% over two steps) as a colorless oil. <sup>1</sup>H NMR (500 MHz, CDCl<sub>3</sub>) δ 7.31–7.26 (m, 4H), 6.87–6.81 (m, 4H), 6.60 (q, *J* = 1.8 Hz, 1H), 4.99–4.89 (m, 1H), 3.79 (s, 6H), 3.74 (s, 3H), 3.68 (d, *J* = 13.8 Hz, 2H), 3.49 (d, *J* = 13.7 Hz, 2H), 3.41 (q, *J* = 7.6 Hz, 1H), 2.73 (ddt, *J* = 16.8, 8.4, 1.8 Hz, 1H), 2.63–2.50 (m, 1H). <sup>13</sup>C NMR (126 MHz, CDCl<sub>3</sub>) δ 165.2, 159.4 (2C), 142.4, 133.3, 130.1 (2C), 128.8 (4C), 114.1 (4C), 69.6, 65.2, 55.5 (2C), 55.4 (2C), 52.0, 30.6. LRMS (APCI) calc. for C<sub>23</sub>H<sub>28</sub>NO<sub>5</sub> [M+H]<sup>+</sup>: 398.20; found, 398.02.

**Methyl *trans*-4-(Bis(4-methoxybenzyl)amino)-3-fluorocyclopent-1-enecarboxylate (20).** To a stirred solution of **19** (1.00 g, 2.52 mmol) in DCM (30 mL) was added Deoxo-Fluor (1.40 mL, 3.77 mmol) dissolved in DCM (20 mL) at −78 °C under an argon atmosphere. The resulting mixture was warmed to room temperature and stirred overnight. After the completion of the reaction, the solution was quenched with water and extracted with DCM (25 mL × 3). The combined organic layers were separated, washed with sat. Na<sub>2</sub>CO<sub>3</sub> solution and brine, dried over Na<sub>2</sub>SO<sub>4</sub>, and concentrated under vacuum conditions. The crude product was purified via Combi-Flash chromatography (EtOAc/hexane: 0–100%) to yield **20** (0.26 g, 26%) as a colorless oil. <sup>1</sup>H NMR (500 MHz, CDCl<sub>3</sub>) δ 7.35–7.18 (m, 4H), 6.92–6.78 (m, 4H), 6.64 (s, 1H), 5.77 (dd, *J* = 53.6, 2.4 Hz, 1H), 3.80 (s, 6H), 3.76 (s, 3H), 3.72–3.65 (m, 1H), 3.56 (s, 4H), 2.88–2.76 (m, 1H), 2.63–2.51 (m, 1H). <sup>13</sup>C NMR (126 MHz, CDCl<sub>3</sub>) δ 164.8, 158.9 (2C), 139.75 (d, *J* = 9.4 Hz), 137.72 (d, *J* = 19.4 Hz), 131.1 (2C), 129.9 (4C), 113.8 (4C), 98.79 (d, *J* = 177.7 Hz), 66.18 (d, *J* = 20.8 Hz), 55.4 (2C), 54.4 (2C), 52.1, 32.52 (d, *J* = 4.1 Hz). LRMS (APCI) calc. for C<sub>23</sub>H<sub>27</sub>FO<sub>5</sub> [M+H]<sup>+</sup>: 400.19; found, 400.14.

**Methyl *trans*-4-((*tert*-Butoxycarbonyl)amino)-3-fluorocyclopent-1-enecarboxylate (21)** (i) To a stirred solution of **20** (0.33 g, 0.829 mmol) in CH<sub>3</sub>CN (15 mL) was added ceric ammonium nitrate (3.634 g, 6.63 mmol) dissolved in H<sub>2</sub>O (5 mL) at 0 °C. The resulting mixture was stirred at room temperature for 3 h. After the completion of the reaction, the solution was diluted with EtOAc (50 mL) and NaHCO<sub>3</sub> (sat., aq.) and stirred vigorously until the pH of the aqueous layer was 8. The suspension was filtered through a Celite pad and washed with EtOAc. The filtrate was then concentrated under vacuum conditions to afford a solution (presumed aqueous from residual water) containing deprotected product. This crude product was used directly in the next step without further purification. (ii) To a stirred solution of the crude product (theoretically 0.132 g, 0.829 mmol) in MeOH (9 mL) was added Boc<sub>2</sub>O (0.271 g, 1.24 mmol). The resulting mixture was stirred at room temperature overnight. After the completion of the reaction, the remaining solvent was concentrated under vacuum conditions and via Combi-Flash chromatography (EtOAc/hexane: 0–100%) to afford **21** as a colorless oil (60 mg, 28%). <sup>1</sup>H NMR (500 MHz, CDCl<sub>3</sub>) δ 6.65 (t, *J* = 2.2 Hz, 1H), 5.61 (d, *J* = 53.4 Hz, 1H), 4.80 (br s, 1H),

4.29–4.14 (m, 1H), 3.77 (s, 3H), 3.18–3.04 (m, 1H), 2.51 (s, 1H), 1.45 (s, 9H).  $^{13}\text{C}$  NMR (126 MHz,  $\text{CDCl}_3$ )  $\delta$  164.5, 155.3, 139.76 (d,  $J = 9.6$  Hz), 136.86 (d,  $J = 18.7$  Hz), 101.25 (d,  $J = 180.6$  Hz), 80.3, 57.35 (d,  $J = 24.9$  Hz), 52.2, 36.7, 28.5 (3C). LRMS (APCI) calc. for  $\text{C}_7\text{H}_{10}\text{FNO}_2$   $[\text{M}-\text{Boc}+\text{H}]^+$ : 159.07; found, 159.99.

***trans*-4-Amino-3-fluorocyclopent-1-enecarboxylic acid hydrochloride (6).** To a stirred solution of **21** (30 mg, 0.72 mmol) in acetic acid (7 mL) was added 4N HCl (7 mL) at room temperature. The resulting mixture was heated at 70 °C overnight. After the completion of the reaction, the excess solvent was removed under vacuum conditions. The crude product was purified via Combi-Flash chromatography (C18 reverse-phase column,  $\text{CH}_3\text{CN}/\text{H}_2\text{O}$ : 0–5%) to give **6** as a white powder HCl salt (5 mg, 24%).  $^1\text{H}$  NMR (500 MHz,  $\text{D}_2\text{O}$ )  $\delta$  6.69 (dq,  $J = 4.1, 2.2$  Hz, 1H), 5.90 (dddt,  $J = 52.3, 3.2, 2.3, 1.0$  Hz, 1H), 4.14 (dddd,  $J = 23.8, 8.5, 5.5, 4.2$  Hz, 1H), 3.33–3.17 (m, 1H), 2.73–2.55 (m, 1H).  $^{13}\text{C}$  NMR (126 MHz,  $\text{D}_2\text{O}$ )  $\delta$  167.8, 140.51 (d,  $J = 9.6$  Hz), 135.12 (d,  $J = 19.7$  Hz), 99.25 (d,  $J = 178.3$  Hz), 55.40 (d,  $J = 26.1$  Hz), 34.4. HRMS (ESI) calc. for  $\text{C}_6\text{H}_9\text{FNO}_2$   $[\text{M}+\text{H}]^+$ : 146.0612; found, 146.0613.

### 3.2. Expression and Purification of hOAT

hOAT was expressed and purified using previously published protocols [18]. Briefly, *E. coli* BL21(DE3) cells, containing the pMAL-t-hOAT plasmid, were incubated at 37 °C with shaking in a lysogeny broth (LB) medium supplemented with 100  $\mu\text{g}/\text{mL}$  ampicillin. When the culture  $\text{OD}_{600}$  reached a value of 0.7, expression of the MBP-t-hOAT fusion protein was induced by the addition of 0.3 mM isopropyl  $\beta$ -D-1-thiogalactopyranoside and further incubated for an additional 16–18 h at 25 °C. Cells were harvested by centrifugation, washed with buffer A comprised of 20 mM Tris-HCl, 200 mM NaCl, and 100  $\mu\text{M}$  PLP, pH 7.4, and flash-frozen in liquid nitrogen and stored at  $-80$  °C. The frozen cell pellet was then thawed, sonicated in buffer A, and centrifuged at  $40,000\times g$  for 20 min. The resulting supernatant was loaded onto an amylose affinity column pre-equilibrated with buffer A. The column was washed thoroughly, and the MBP-t-hOAT fusion protein was eluted from the column with 10 mM maltose. Fractions containing the fusion protein were combined and treated with TEV protease to remove the MBP tag. The cleaved hOAT protein was collected and concentrated using a centrifugal filter. The protein was then further purified by size exclusion chromatography using a HiLoad Superdex-200PG column. The column was pre-equilibrated, and the protein eluted in buffer containing 50 mM HEPES, 100  $\mu\text{M}$  PLP, and 300 mM NaCl, pH 7.5.

### 3.3. Aminotransferases and Coenzymes for Kinetic Studies

All reagents for enzyme purification and assays were purchased from Sigma-Aldrich (St. Louis, MO, USA). Human OAT (0.672 mg/mL) was purified from *E. coli* BL21 (DE3) cells following the procedure described above, and coenzyme human recombinant pyrroline 5-carboxylate reductase (PYCR1) was expressed, grown, and purified according to a procedure outlined in the literature [30].  $\gamma$ -Aminobutyric acid aminotransferase (GABA-AT, 0.4 mg/mL) was purified from pig brain following a procedure described previously [31], and coenzyme succinic semialdehyde dehydrogenase (SSDH) was purified from GABase (catalog No. G7509-25UN, Sigma-Aldrich), a commercially available mixture of SSDH and GABA-AT, using a known procedure [32]. Coupled enzyme assays for GABA-AT and hOAT were carried out according to previous procedures [33,34]. All of the enzyme assays for the inactivation, partition ratio, and dialysis experiment were recorded on a Synergy H1 hybrid multimode microplate reader (Biotek, USA) with transparent 96-well plates.

### 3.4. Denaturing Intact Protein and Small Molecule Mass Spectrometry

Treated and unmodified purified hOAT samples were desalted ten times with Optima-grade water (Fisher) on Amicon Ultra 10 kDa molecular weight spin filters

(Millipore). To chromatographically resolve protein, 0.5 µg of protein was loaded onto a 3 cm PLRP-S (Agilent) trap column using a Dionex Ultimate3000 liquid chromatography system (Thermo Fisher). The protein analyte was washed with a 10 min isocratic gradient of 10% Solvent B (95% acetonitrile/5% H<sub>2</sub>O/0.2% formic acid) and 90% Solvent A (5% acetonitrile/95% H<sub>2</sub>O/0.2% formic acid). Protein was resolved on an in-house-made 75 µm ID × 15 cm long nanopore capillary column packed with PLRP-S resin (Agilent). The LC system was operated at a flow rate of 0.3 µL/min at the following gradient: 0–10 min 10% Solvent B; 10–12 min to 40% Solvent B; 12–22 min to 90% Solvent B; 22–24 min at 90% Solvent B; 24–26 min to 10% Solvent B; 26–30 min isocratic at 10% Solvent B. *h*OAT samples were introduced into a Thermo Fisher Orbitrap Fusion Lumos or Eclipse mass spectrometer, and full MS data were acquired as previously described [28]. Small molecule *h*OAT substrate and product masses were identified and characterized by positive and negative mode high-resolution LC-MS/MS on a Q-Exactive Orbitrap mass spectrometer (Thermo), as previously described [13,14,28].

### 3.5. Theoretical $pK_a$ Calculations

Theoretical  $pK_a$  calculations were conducted following a procedure described previously [14,26]. The geometries of the neutral and deprotonated species of **M15**, **M15-1**, and **M15-2** were fully optimized using the DFT B3LYP/6-31G\*\* level of theory. For all of the investigated compounds, the gas-phase Gibbs free energy changes ( $\Delta G_g^\circ$ ) of compounds were calculated using Gaussian09 software [35]. The solvation free energies were calculated by applying polarizable continuum model (PCM), using the same level of theory and basis set (B3LYP/6-31G\*\*) which was used for geometry determination in the gas phase. The PCM calculations were used with the UAHF atomic radii when building the solvent cavity to calculate the Gibbs free energy of solvation. The  $pK_a$  values were obtained applying the following Equations (1)–(3) and the thermodynamic cycle A, presented by Ghalami-Chooabar and coworkers [25].

$$\Delta G_{aq}^\circ = \Delta G_g^\circ + \Delta G_s^\circ \quad (1)$$

$$\Delta G_{aq}^\circ = -2.303RT \log K_a \quad (2)$$

$$\Delta G_{aq}^\circ = \Delta G_g^\circ(A^-) + \Delta G_s^\circ(H^+) - \Delta G_s^\circ(AH) + G_g^\circ(A^-) + G_s^\circ(H^+) - G_s^\circ(AH) \quad (3)$$

### 3.6. Electrostatic Potential (ESP) Charge Calculation

The three-dimensional (3D) molecular models of **M18**, **M18-1**, and **M18-2** were built up using Spartan'14 software (Wavefunction, Inc., 2014, Irvine, United States). The build structures were refined by molecular mechanics using Merck molecular force field (MMFF94). Then, with the lowest energy conformer selected, the equilibrium geometry and molecular orbitals were calculated using Hartree–Fock (HF) at the 6-31G\* level of theory. Spartan'14 was also used to generate electron density and electrostatic potential maps.

### 3.7. Co-Crystallization of *h*OAT with Compound 5

**Crystal Growth.** The freshly prepared enzyme was dialyzed with 50 mM potassium pyrophosphate which contained 5 mM  $\alpha$ -ketoglutarate at pH 8.0 overnight. The enzyme was then incubated with excess amount of compound **5** at 4 °C overnight. The pre-inactivated *h*OAT sample was buffer exchanged into 50 mM Tricine pH 7.8 and concentrated to a protein concentration of 6 mg/mL. Previously reported crystallization conditions [28] were optimized using the hanging drop vapor diffusion method by varying PEG 6000 (8–12%), NaCl (100–250 mM), glycerol (0–10%) with 100 mM Tricine pH 7.8 as the buffer. For each hanging drop, either 2 or 3 µL of protein solution was mixed with equal volume of well solution. Several rounds of seeding followed to improve crystal size and quality. The crystals with the best morphology and size grew in a final condition

containing 10% PEG 6000, 100 mM NaCl, 10% glycerol, 100 mM Tricine pH 7.8 at the temperature of 20 °C (293 K). Crystals were transferred to a cryo-protectant solution (well solution supplemented with 30% glycerol) before being flash-frozen in liquid nitrogen.

**X-ray Diffraction and Data Processing.** Monochromatic X-ray diffraction data were collected at the LS-CAT beamline 21-ID-D at the Advanced Photon Source at Argonne National Laboratory. Data were collected at a wavelength of 1.127 Å and a temperature of 100 K using a Dectris Eiger 9M detector. Datasets were processed and analyzed with autoPROC software [36].

**Model Building and Refinement.** The *h*OAT structure was solved by molecular replacement using PHASER [37] in Phenix. The starting search model was the previously published structure of *h*OAT (PDB code: 1OAT [27]). The model building and refinement were accomplished in Coot [38] and Phenix [39], respectively, as an iterative process until the lowest possible  $R_{\text{free}}/R$  factor values were attained. Structural depiction figures were prepared using UCSF Chimera [40].

### 3.8. Transient-State Methods

The reaction of **5** with OAT was observed in a transient state using stopped-flow spectrophotometry (TgK Scientific). Solutions were mixed in a 1:1 ratio, and spectrophotometric data were collected using a charged coupled device for wavelengths (260–800 nm). To capture data with temporal resolution that adequately described both fast and slow chemical steps, duplicate datasets were collected using a log time base for two timeframes (0.0025–5 seconds and 0.0025–1250 seconds). The duplicate datasets for any one timeframe were averaged and the data for both time frames were spliced together at 5 seconds to form one dataset. In these experiments, 13.4 µM *h*OAT was allowed to react with varied concentrations of **5** (62, 123, 245, 490, 980, 1960, 3920 and 7830 µM) in 50 mM HEPES, 200 mM NaCl, pH 7.5 at 10 °C (all concentration indicated are post-mixing). Reaction traces at specific wavelengths were extracted from the spectral data and combined into single datasets that depict the concentration dependence of the processes observed. These data were fit analytically to a linear combination of exponentials (Equation (4)) to evaluate concentration dependences. In this equation,  $A_{xnm}$  is the absorbance at any time,  $\Delta A_n$  is the amplitude associated with phase  $n$ ,  $k_n$  is the rate constant for phase  $n$ , and  $C$  is the absorption at infinite time. The dependencies of observed rate constants were fit to Equation (5) for reversible steps and to Equation (6) for irreversible steps that follow reversible steps. In these equations  $k_{\text{obs}}$  is the observed rate constant,  $k_n$  is the limiting value of the forward rate constant,  $[5]$  is the concentration of inhibitor, and  $K_{\text{eq}}$  is the equilibrium constant for the preceding step. Hybrid timeframe CCD spectral datasets, collected at a concentration of **5** equal to 1960 µM, were fit globally to an irreversible linear four-step model using the Spectrafit singular value decomposition (SVD) module of the KinTek Explorer software. This concentration was selected to avoid the enzyme precipitation that was evident in the data collected for 3920 and 7830 µM of **5**.

$$A_{xnm} = \Delta A_1(e^{-k_1t}) + \Delta A_2(e^{-k_2t}) + \Delta A_3(e^{-k_3t}) + C \quad (4)$$

$$k_{\text{obs}} = k_{-n} + \frac{k_n[5]}{(1/K_{\text{eq}} + [5])} \quad (5)$$

$$k_{\text{obs}} = \frac{k_n[5]}{(1/K_{\text{eq}} + [5])} \quad (6)$$

### 3.9. Gibb's Free Energy Calculation

MOPAC 2016 is a computational chemistry software that is based on the concepts of quantum theory and thermodynamics, using some concepts of advanced mathematics. It is a semi-empirical molecular orbital package used for the study of solid-state nanostructure molecular structures, and their reactions [41]. In this context, MOPAC 2016

has been used for setting the molecular geometries of each tautomeric form in Figure 9B, followed by optimization through the PM7 semi-empirical method. Solvation by water molecules was not considered for the calculation. A combination of molecular mechanics energy, polar and nonpolar energies, and entropy have been considered for the resulting binding free energy of each tautomer presented in Figure 9B. Enthalpy ( $\Delta H^\circ$ ) and entropy ( $\Delta S^\circ$ ) contribute to the  $\Delta G^\circ$  value of each tautomer, something also determined by the Gibb's free energy equation:

$$\Delta G^\circ = \Delta H^\circ - T\Delta S^\circ \quad (7)$$

### 3.10. Molecular Docking Protocol

Molecular docking studies were conducted following a procedure described previously [13,26]. Docking models of ligands bound to *h*OAT were developed using the Molecular Operating Environment (MOE) computational suite's Builder utility [42]. The energy minimization of ligands was conducted in the gas phase using the force field MMFF94X, followed by the Conformational Search protocol to generate structural-conformation databases. The X-ray crystal structures of native *h*OAT (1OAT) and inactivated *h*OAT (1GBN) were uploaded to MOE, followed by the use of the Receptor Preparation step. The tight-binding product in the active pocket was deleted, and catalytic Lys292 was neutralized. The docking site was specified by the Lys292-PLP linkage. Ligand docking simulation was carried out in the prepared aminotransferase enzyme models with unrelated substrates and the solvent atoms inactivated. Ligand placement employed the Alpha Triangle method with Affinity  $\Delta G$  scoring, generating 300 data points that were further refined using the induced fit method with GBVI/WSA  $\Delta G$  scoring to obtain the top 50 docking results. The docking results of each ligand were analyzed for selection of the best docking pose, based on the score and reported X-ray structures. All renderings were then performed in MOE. The PLP moieties of the docked molecules (Figure 9A) showed comparable docking poses with our previous findings [13,14], while carboxylate groups formed tight interactions with Arg180, indicating reasonable docking poses in the active site of *h*OAT.

## 4. Conclusions

The incorporation of a double bond into a cyclopentane system has significantly improved the inactivation efficiency of our recent MBIs by enhancing the reactivity of the key  $C_\gamma$  hydrogen and providing conformational changes [26,43–45]. In this work, we carried out an integrated mechanistic study with *h*OAT and **5**, demonstrating that the addition of a double bond also influences the inactivation mechanism pathways. Unlike the parent monofluorinated cyclopentane (**4**), showing a typical enamine addition mechanism, the  $\alpha$ ,  $\beta$ -unsaturated cyclopentene **5** mainly inactivates *h*OAT through noncovalent, tight-binding interactions. This has been fully characterized by intact protein MS, wavelength absorbance measurements of the final products, and co-crystallization. The co-crystal complex also reveals for the first time that, in both the minor covalent and major noncovalent forms, the carboxylate group of **5** establishes unusual salt bridges with Arg413 rather than salt bridges with Arg180/Tyr55, as was previously observed in all the co-crystals of *h*OAT with other MBIs [14,26,28,45]. The transition state kinetics further indicate that a secondary external aldimine is formed between the first external aldimine and the first quinonoid transitions. Supported by molecular docking and free energy calculations, we propose the potential existence of an enolate intermediate that might be converted from the carboxylate of **5** and participate in the inactivation cascade directly. Overall, compound **5** inactivates *h*OAT through a unique enamine addition mechanism. These results will aid in the future design of selective *h*OAT inactivators.

**Supplementary Materials:** The following supporting information can be downloaded at: [www.mdpi.com/article/10.3390/molecules28031133/s1](http://www.mdpi.com/article/10.3390/molecules28031133/s1), Figure S1: Primary metabolite **Met II** of **5** in *h*OAT; Figure S2: The asymmetric unit of the co-crystal structure of *h*OAT inactivated by **5**; Figure S3: The biological assembly of *h*OAT represents a homodimer; Table S1: Statistics of the crystal structures of *h*OAT inactivated by **5**.

**Author Contributions:** S.S. and A.B. contributed equally to this work. S.S. carried out most of the synthetic and biochemical experiments and molecular docking studies, and wrote the initial draft of the manuscript; A.B. purified the *h*OAT and performed the crystallographic studies; A.B. and B.A.B. conducted transition state measurements; G.M.F. carried out computational calculations ( $pK_a$ , ESP, free energies); P.F.D. performed all of the mass spectral experiments and interpreted the data; D.H.G. and W.Z. synthesized compound **6**; N.L.K. directed the mass spectrometry experiments; G.R.M. directed the transition state measurements and drafted up the corresponding sections; D.L. directed the crystallographic studies; and R.B.S. directed the chemistry work and edited the drafts of the manuscript. All authors have read and edited the manuscript and have given their approval of the final version. All authors have read and agreed to the published version of the manuscript.

**Funding:** We are grateful to the National Institutes of Health (Grants R01 DA030604 and R01 CA260250 to R.B.S. and Grant P30 DA018310 to N.L.K.) and the National Science Foundation (Grant 2015210477 to P.F.D. and Grant 1904480 to G.R.M.) for financial support. This work used the Extreme Science and Engineering Discovery Environment (XSEDE) Comet Bridges Stampede2 through allocation TG-CHE190070, which is supported by National Science Foundation grant number ACI-1548562. This work made use of the IMSERC at Northwestern University, which has received support from the Soft and Hybrid Nanotechnology Experimental (SHyNE) Resource (NSF NNCI-1542205), the State of Illinois, and the International Institute for Nanotechnology (IIN). X-ray diffraction data collection used resources of the Advanced Photon Source, a U.S. Department of Energy (DOE) Office of financial support. Science User Facility operated for the DOE Office of Science by Argonne National Laboratory under contract no. DEAC02-06CH11357. The use of LS-CAT Sector 21 was supported by the Michigan Economic Development Corporation and the Michigan Technology Tri-Corridor (grant 085P1000817). G.M.F. is a recipient of a fellowship from FAPESP, Brazil.

**Institutional Review Board Statement:** Not applicable.

**Informed Consent Statement:** Not applicable.

**Data Availability Statement:** Not applicable.

**Conflicts of Interest:** The authors declare no conflict of interest.

**Sample Availability:** Samples of compounds **1–9** are available on reasonable request from the authors.

## References

1. Jansonius, J.N. Structure, evolution and action of vitamin B6-dependent enzymes. *Curr. Opin. Struct. Biol.* **1998**, *8*, 759–769. [https://doi.org/10.1016/S0959-440X\(98\)80096-1](https://doi.org/10.1016/S0959-440X(98)80096-1).
2. Hwang, B.-Y.; Cho, B.-K.; Yun, H.; Koteswarar, K.; Kim, B.-G. Revisit of aminotransferase in the genomic era and its application to biocatalysis. *J. Mol. Catal. B Enzym.* **2005**, *37*, 47–55. <https://doi.org/10.1016/j.molcatb.2005.09.004>.
3. Silverman, R.B. Design and Mechanism of GABA Aminotransferase Inactivators. Treatments for Epilepsies and Addictions. *Chem. Rev.* **2018**, *118*, 4037–4070. <https://doi.org/10.1021/acs.chemrev.8b00009>.
4. Yogeewari, P.; Sriram, D.; Vaigundaragavendran, J. The GABA shunt: An attractive and potential therapeutic target in the treatment of epileptic disorders. *Curr. Drug Metab.* **2005**, *6*, 127–139. <https://doi.org/10.2174/1389200053586073>.
5. Lee, H.; Juncosa, J.I.; Silverman, R.B. Ornithine aminotransferase versus GABA aminotransferase: Implications for the design of new anticancer drugs. *Med. Res. Rev.* **2015**, *35*, 286–305. <https://doi.org/10.1002/med.21328>.
6. Zigmond, E.; Ben Ya'acov, A.; Lee, H.; Lichtenstein, Y.; Shalev, Z.; Smith, Y.; Zolotarov, L.; Ziv, E.; Kalman, R.; Le, H.V.; et al. Suppression of Hepatocellular Carcinoma by Inhibition of Overexpressed Ornithine Aminotransferase. *ACS Med. Chem. Lett.* **2015**, *6*, 840–844. <https://doi.org/10.1021/acsmedchemlett.5b00153>.
7. Liu, Y.; Wu, L.; Li, K.; Liu, F.; Wang, L.; Zhang, D.; Zhou, J.; Ma, X.; Wang, S.; Yang, S. Ornithine aminotransferase promoted the proliferation and metastasis of non-small cell lung cancer via upregulation of miR-21. *J. Cell. Physiol.* **2019**, *234*, 12828–12838. <https://doi.org/10.1002/jcp.27939>.
8. Foroozan, R. Vigabatrin: Lessons Learned From the United States Experience. *J. Neuroophthalmol.* **2018**, *38*, 442–450. <https://doi.org/10.1097/WNO.0000000000000609>.



9. Silverman, R.B. Mechanism-based enzyme inactivators. *Methods Enzymol.* **1995**, *249*, 240–283. [https://doi.org/10.1016/0076-6879\(95\)49038-8](https://doi.org/10.1016/0076-6879(95)49038-8).
10. Nanavati, S.M.; Silverman, R.B. Mechanisms of inactivation of  $\gamma$ -aminobutyric acid aminotransferase by the antiepilepsy drug  $\gamma$ -vinyl GABA (vigabatrin). *J. Am. Chem. Soc.* **1991**, *113*, 9341–9349. <https://doi.org/10.1021/ja00024a043>.
11. Silverman, R.B.; Levy, M.A. Mechanism of inactivation of  $\gamma$ -aminobutyric acid- $\alpha$ -ketoglutaric acid aminotransferase by 4-amino-5-halopentanoic acids. *Biochemistry* **1981**, *20*, 1197–1203. <https://doi.org/10.1021/bi00508a022>.
12. Silverman, R.B.; Invergo, B.J. Mechanism of inactivation of  $\gamma$ -aminobutyrate aminotransferase by 4-amino-5-fluoropentanoic acid. First example of an enamine mechanism for a  $\gamma$ -amino acid with a partition ratio of 0. *Biochemistry* **1986**, *25*, 6817–6820. <https://doi.org/10.1021/bi00370a013>.
13. Shen, S.; Doubleday, P.F.; Weerawarna, P.M.; Zhu, W.; Kelleher, N.L.; Silverman, R.B. Mechanism-Based Design of 3-Amino-4-Halocyclopentenecarboxylic Acids as Inactivators of GABA Aminotransferase. *ACS Med. Chem. Lett.* **2020**, *11*, 1949–1955. <https://doi.org/10.1021/acsmmedchemlett.9b00672>.
14. Zhu, W.; Doubleday, P.F.; Catlin, D.S.; Weerawarna, P.M.; Butrin, A.; Shen, S.; Wawrzak, Z.; Kelleher, N.L.; Liu, D.; Silverman, R.B. A Remarkable Difference That One Fluorine Atom Confers on the Mechanisms of Inactivation of Human Ornithine Aminotransferase by Two Cyclohexene Analogues of  $\gamma$ -Aminobutyric Acid. *J. Am. Chem. Soc.* **2020**, *142*, 4892–4903. <https://doi.org/10.1021/jacs.0c00193>.
15. Wang, Z.; Silverman, R.B. Syntheses and evaluation of fluorinated conformationally restricted analogues of GABA as potential inhibitors of GABA aminotransferase. *Bioorg. Med. Chem.* **2006**, *14*, 2242–2252. <https://doi.org/10.1016/j.bmc.2005.11.010>.
16. Storici, P.; Capitani, G.; Muller, R.; Schirmer, T.; Jansonius, J.N. Crystal structure of human ornithine aminotransferase complexed with the highly specific and potent inhibitor 5-fluoromethylornithine. *J. Mol. Biol.* **1999**, *285*, 297–309. <https://doi.org/10.1006/jmbi.1998.2289>.
17. Silverman, R.B.; George, C. Mechanism of inactivation of  $\gamma$ -aminobutyric acid aminotransferase by (S,E)-4-amino-5-fluoropent-2-enoic acid. *Biochem. Biophys. Res. Commun.* **1988**, *150*, 942–946. [https://doi.org/10.1016/0006-291X\(88\)90720-6](https://doi.org/10.1016/0006-291X(88)90720-6).
18. Mascarenhas, R.; Le, H.V.; Clevenger, K.D.; Lehrer, H.J.; Ringe, D.; Kelleher, N.L.; Silverman, R.B.; Liu, D. Selective Targeting by a Mechanism-Based Inactivator against Pyridoxal 5'-Phosphate-Dependent Enzymes: Mechanisms of Inactivation and Alternative Turnover. *Biochemistry* **2017**, *56*, 4951–4961. <https://doi.org/10.1021/acs.biochem.7b00499>.
19. Storici, P.; Qiu, J.; Schirmer, T.; Silverman, R.B. Mechanistic crystallography. Mechanism of inactivation of  $\gamma$ -aminobutyric acid aminotransferase by (1R,3S,4S)-3-amino-4-fluorocyclopentane-1-carboxylic acid as elucidated by crystallography. *Biochemistry* **2004**, *43*, 14057–14063. <https://doi.org/10.1021/bi0487185>.
20. Bey, P.; Gerhart, F.; Jung, M. Synthesis of (E)-4-amino-2,5-hexadienoic acid and (E)-4-amino-5-fluoro-2-pentenoic acid. Irreversible inhibitors of 4-aminobutyrate-2-oxoglutarate aminotransferase. *J. Org. Chem.* **1986**, *51*, 2835–2838. <https://doi.org/10.1021/jo00364a049>.
21. Bolkenius, F.N.; Knodgen, B.; Seiler, N. DL-canaline and 5-fluoromethylornithine. Comparison of two inactivators of ornithine aminotransferase. *Biochem. J.* **1990**, *268*, 409–414. <https://doi.org/10.1042/bj2680409>.
22. Qiu, J.; Silverman, R.B. A new class of conformationally rigid analogues of 4-amino-5-halopentanoic acids, potent inactivators of  $\gamma$ -aminobutyric acid aminotransferase. *J. Med. Chem.* **2000**, *43*, 706–720. <https://doi.org/10.1021/jm9904755>.
23. Smith, M.E.B.; Derrien, N.; Lloyd, M.C.; Taylor, S.J.C.; Chaplin, D.A.; McCague, R. Highly selective directed hydrogenation of enantiopure 4-(tert-butoxycarbonylamino)cyclopent-1-enecarboxylic acid methyl esters. *Tetrahedron Lett.* **2001**, *42*, 1347–1350. [https://doi.org/10.1016/S0040-4039\(00\)02210-3](https://doi.org/10.1016/S0040-4039(00)02210-3).
24. Zhang, H.; Schinazi, R.F.; Chu, C.K. Synthesis of neplanocin F analogues as potential antiviral agents. *Bioorganic Med. Chem.* **2006**, *14*, 8314–8322. <https://doi.org/10.1016/j.bmc.2006.09.007>.
25. Ghalami-Choobar, B.; Dezhmanpanah, H.; Nikparsa, P.; Ghiami-Shomami, A. Theoretical calculation of the pKa values of some drugs in aqueous solution. *Int. J. Quantum Chem.* **2012**, *112*, 2275–2280. <https://doi.org/10.1002/qua.23211>.
26. Shen, S.; Butrin, A.; Doubleday, P.F.; Melani, R.D.; Beaupre, B.A.; Tavares, M.T.; Ferreira, G.M.; Kelleher, N.L.; Moran, G.R.; Liu, D.; et al. Turnover and Inactivation Mechanisms for (S)-3-Amino-4,4-difluorocyclopent-1-enecarboxylic Acid, a Selective Mechanism-Based Inactivator of Human Ornithine Aminotransferase. *J. Am. Chem. Soc.* **2021**, *143*, 8689–8703. <https://doi.org/10.1021/jacs.1c02456>.
27. Shen, B.W.; Hennig, M.; Hohenester, E.; Jansonius, J.N.; Schirmer, T. Crystal structure of human recombinant ornithine aminotransferase. *J. Mol. Biol.* **1998**, *277*, 81–102. <https://doi.org/10.1006/jmbi.1997.1583>.
28. Moschitto, M.J.; Doubleday, P.F.; Catlin, D.S.; Kelleher, N.L.; Liu, D.; Silverman, R.B. Mechanism of Inactivation of Ornithine Aminotransferase by (1S,3S)-3-Amino-4-(hexafluoropropan-2-ylidenyl)cyclopentane-1-carboxylic Acid. *J. Am. Chem. Soc.* **2019**, *141*, 10711–10721. <https://doi.org/10.1021/jacs.9b03254>.
29. Moschitto, M.J.; Silverman, R.B. Synthesis of (S)-3-Amino-4-(difluoromethylenyl)-cyclopent-1-ene-1-carboxylic Acid (OV329), a Potent Inactivator of  $\gamma$ -Aminobutyric Acid Aminotransferase. *Org. Lett.* **2018**, *20*, 4589–4592. <https://doi.org/10.1021/acs.orglett.8b01872>.
30. Christensen, E.M.; Patel, S.M.; Korasick, D.A.; Campbell, A.C.; Krause, K.L.; Becker, D.F.; Tanner, J.J. Resolving the cofactor-binding site in the proline biosynthetic enzyme human pyrroline-5-carboxylate reductase 1. *J. Biol. Chem.* **2017**, *292*, 7233–7243. <https://doi.org/10.1074/jbc.M117.780288>.
31. Koo, Y.K.; Nandi, D.; Silverman, R.B. The multiple active enzyme species of  $\gamma$ -aminobutyric acid aminotransferase are not isozymes. *Arch. Biochem. Biophys.* **2000**, *374*, 248–254. <https://doi.org/10.1006/abbi.1999.1623>.

- 
32. Silverman, R.B.; Bichler, K.A.; Leon, A.J.J. Mechanisms of inactivation of  $\gamma$ -aminobutyric acid aminotransferase by 4-amino-5-fluoro-5-hexenoic acid. *Am. Chem. Soc.* **1996**, *118*, 1241–1252.
  33. Lee, H.; Doud, E.H.; Wu, R.; Sanishvili, R.; Juncosa, J.I.; Liu, D.; Kelleher, N.L.; Silverman, R.B. Mechanism of inactivation of gamma-aminobutyric acid aminotransferase by (1S,3S)-3-amino-4-difluoromethylene-1-cyclopentanoic acid (CPP-115). *J. Am. Chem. Soc.* **2015**, *137*, 2628–2640. <https://doi.org/10.1021/ja512299n>.
  34. Juncosa, J.I.; Lee, H.; Silverman, R.B. Two continuous coupled assays for ornithine-delta-aminotransferase. *Anal. Biochem.* **2013**, *440*, 145–149. <https://doi.org/10.1016/j.ab.2013.05.025>.
  35. Official Gaussian 09 Literature Citation. Available online: [http://sobereva.com/g09/m\\_citation](http://sobereva.com/g09/m_citation). (accessed on 18 January 2023)
  36. Vonrhein, C.; Flensburg, C.; Keller, P.; Sharff, A.; Smart, O.; Paciorek, W.; Womack, T.; Bricogne, G. Data processing and analysis with the autoPROC toolbox. *Acta Cryst. D Biol. Cryst.* **2011**, *67* (Pt 4), 293–302. <https://doi.org/10.1107/S0907444911007773>.
  37. McCoy, A.J.; Grosse-Kunstleve, R.W.; Adams, P.D.; Winn, M.D.; Storoni, L.C.; Read, R.J. Phaser crystallographic software. *J. Appl. Cryst.* **2007**, *40* (Pt 4), 658–674. <https://doi.org/10.1107/S0021889807021206>.
  38. Emsley, P.; Lohkamp, B.; Scott, W.G.; Cowtan, K. Features and development of Coot. *Acta Cryst. D Biol. Cryst.* **2010**, *66* (Pt 4), 486–501. <https://doi.org/10.1107/S0907444910007493>.
  39. Liebschner, D.; Afonine, P.V.; Baker, M.L.; Bunkoczi, G.; Chen, V.B.; Croll, T.I.; Hintze, B.; Hung, L.W.; Jain, S.; McCoy, A.J.; et al. Macromolecular structure determination using X-rays, neutrons and electrons: Recent developments in Phenix. *Acta Cryst. D Struct. Biol.* **2019**, *75* (Pt 10), 861–877. <https://doi.org/10.1107/S2059798319011471>.
  40. Pettersen, E.F.; Goddard, T.D.; Huang, C.C.; Couch, G.S.; Greenblatt, D.M.; Meng, E.C.; Ferrin, T.E. UCSF Chimera—a visualization system for exploratory research and analysis. *J. Comput. Chem.* **2004**, *25*, 1605–1612. <https://doi.org/10.1002/jcc.20084>.
  41. Stewart, J.J.P. Optimization of parameters for semiempirical methods VI: More modifications to the NDDO approximations and re-optimization of parameters. *J. Mol. Model.* **2013**, *19*, 1–32. <https://doi.org/10.1007/s00894-012-1667-x>.
  42. Vilar, S.; Cozza, G.; Moro, S. Medicinal Chemistry and the Molecular Operating Environment (MOE): Application of QSAR and Molecular Docking to Drug Discovery. *Curr. Top. Med. Chem.* **2008**, *8*, 1555–1572. <https://doi.org/10.2174/156802608786786624>.
  43. Juncosa, J.I.; Takaya, K.; Le, H.V.; Moschitto, M.J.; Weerawarna, P.M.; Mascarenhas, R.; Liu, D.L.; Dewey, S.L.; Silverman, R.B. Design and Mechanism of (S)-3-Amino-4-(difluoromethylenyl)cyclopent-1-ene-1-carboxylic Acid, a Highly Potent gamma-Aminobutyric Acid Aminotransferase Inactivator for the Treatment of Addiction. *J. Am. Chem. Soc.* **2018**, *140*, 2151–2164. <https://doi.org/10.1021/jacs.7b10965>.
  44. Weerawarna, P.M.; Moschitto, M.J.; Silverman, R.B. Theoretical and Mechanistic Validation of Global Kinetic Parameters of the Inactivation of GABA Aminotransferase by OV329 and CPP-115. *ACS Chem. Biol.* **2021**, *16*, 615–630. <https://doi.org/10.1021/acscchembio.0c00784> From NLM Medline.
  45. Zhu, W.; Butrin, A.; Melani, R.D.; Doubleday, P.F.; Ferreira, G.M.; Tavares, M.T.; Habeeb Mohammad, T.S.; Beaupre, B.A.; Kelleher, N.L.; Moran, G.R.; et al. Rational Design, Synthesis, and Mechanism of (3S,4R)-3-Amino-4-(difluoromethyl)cyclopent-1-ene-1-carboxylic Acid: Employing a Second-Deprotonation Strategy for Selectivity of Human Ornithine Aminotransferase over GABA Aminotransferase. *J. Am. Chem. Soc.* **2022**, *144*, 5629–5642. <https://doi.org/10.1021/jacs.2c00924>.